The Milky Way Tomography with SDSS: III. Stellar Kinematics

Nicholas Bond[1], Željko Ivezić[2], Branimir Sesar[2], Mario Jurić[3], Jeffrey A. Munn[22], Adam Kowalski[2], Sarah Loebman[2], Rok Roškar[2], Timothy C. Beers[7], Julianne Dalcanton[2], Constance M. Rockosi[4], Brian Yanny[5], Heidi J. Newberg[6], Carlos Allende Prieto[9], Ron Wilhelm[10], Young Sun Lee[7], Thirupathi Sivarani[7], Steven R. Majewski[8], John E. Norris[11], Coryn A.L. Bailer-Jones[12], Paola Re Fiorentin[12,13], David Schlegel[14], Alan Uomoto[15], Robert H. Lupton[16], Gillian R. Knapp[16], James E. Gunn[16], Kevin R. Covey[17], J. Allyn Smith[18], Gajus Miknaitis[5], Mamoru Doi,[19], Masayuki Tanaka[20], Masataka Fukugita[21], Steve Kent[5], Douglas Finkbeiner[17], Tom R. Quinn[2], Suzanne Hawley[2], Scott Anderson[2], Furea Kiuchi[2], Alex Chen[2], James Bushong[2], Harkirat Sohi[2], Daryl Haggard[2], Amy Kimball[2], Rosalie McGurk[2], John Barentine[23], Howard Brewington[23], Mike Harvanek[23], Scott Kleinman[23], Jurek Krzesinski[23], Dan Long[23], Atsuko Nitta[23], Stephanie Snedden[23], Brian Lee[14], Jeffrey R. Pier[22], Hugh Harris[22], Jonathan Brinkmann[23], Donald P. Schneider[24], Donald G. York[25]

[1]Physics and Astronomy Department, Rutgers University Piscataway, NJ 08854-8019, U.S.A.

[2]Department of Astronomy, University of Washington, Box 351580, Seattle, WA 98195

[3]Institute for Advanced Study, 1 Einstein Drive, Princeton, NJ 08540

[4]University of California–Santa Cruz, 1156 High St., Santa Cruz, CA 95060

[5]Fermi National Accelerator Laboratory, P.O. Box 500, Batavia, IL 60510

[6]Department of Physics, Applied Physics, and Astronomy, Rensselaer Polytechnic Institute, 110 8th St., Troy, NY 12180

[7]Dept. of Physics & Astronomy, CSCE: Center for the Study of Cosmic Evolution, and JINA: Joint Institute for Nuclear Astrophysics, Michigan State University, East Lansing, MI 48824, USA

[8]Department of Astronomy, University of Virginia, P.O. Box 400325, Charlottesville, VA 22904-4325

[9]McDonald Observatory and Department of Astronomy, University of Texas, Austin, TX 78712

[10]Department of Physics, Texas Tech University, Box 41051, Lubbock, TX 79409

[11]Research School of Astronomy & Astrophysics, The Australian National University, Cotter Road, Weston, ACT 2611, Australia

[12]Max Planck Institut für Astronomie, Königstuhl 17, 69117 Heidelberg, Germany

[13]Department of Physics, University of Ljubljana, Jadranska 19, 1000 Ljubljana, Slovenia

[14]Lawrence Berkeley National Laboratory, One Cyclotron Road, MS 50R5032, Berkeley, CA, 94720

[15]Department of Physics and Astronomy, The John Hopkins University, 3701 San Martin Drive, Baltimore, MD 21218

[16]Princeton University Observatory, Princeton, NJ 08544

[17]Harvard-Smithsonian Center for Astrophysics, 60 Garden Street, Cambridge, MA 02138

[18]Dept. of Physics & Astronomy, Austin Peay State University, Clarksville, TN 37044

[19]Institute of Astronomy, University of Tokyo, 2-21-1 Osawa, Mitaka, Tokyo 181-0015, Japan

[20]Dept. of Astronomy, Graduate School of Science, University of Tokyo, Hongo 7-3-1, Bunkyo-ku, Tokyo, 113-0033, Japan

[21] Institute for Cosmic Ray Research, University of Tokyo, Kashiwa, Chiba, Japan

[22]U.S. Naval Observatory, Flagstaff Station, P.O. Box 1149, Flagstaff, AZ 86002

[23]Apache Point Observatory, 2001 Apache Point Road, P.O. Box 59, Sunspot, NM 88349-0059

[24]Department of Astronomy and Astrophysics, The Pennsylvania State University, University Park, PA 16802

[25]University of Chicago, Astronomy & Astrophysics Center, 5640 S. Ellis Ave., Chicago, IL 60637

ABSTRACT

We study the Milky Way kinematics using a sample of 18.8 million main-sequence stars with $r < 20$ and proper motion measurements derived from SDSS and POSS astrometry. For $\sim$170,000 of these stars radial velocity measurements are also available from the SDSS spectroscopic survey. Distances to stars are determined using a photometric parallax relation, and photometric metallicity estimates are also available for 6.8 million F/G stars. These stars sample a distance range from $\sim$100 pc to 10 kpc, over a quarter of the sky at high galactic latitudes ($|b| > 20°$), and allow a detailed and robust determination of the velocity field as a function of location and metallicity. We find that in the region defined by 1 kpc $< Z < 5$ kpc and 3 kpc $<$ R $<$ 13 kpc, the rotational velocity for disk stars smoothly decreases, and all three components of velocity dispersion increase, with distance from the galactic plane. In contrast, the velocity ellipsoid for halo stars is aligned with spherical coordinate system and spatially invariant within the probed volume. The velocity distribution of nearby ($Z < 1$ kpc) red stars (K/M) is complex and cannot be described by standard Schwarzschild ellipsoid. For stars in a distance-limited subsample equivalent to HIPPARCOS sample ($<$100 pc), we detect multimodal distribution consistent with HIPPARCOS results and similar to Eggen's moving groups. This strong non-gaussianity significantly affects the measurements of velocity ellipsoid tilt and vertex deviation when using the Schwarzschild approximation. We develop and test a relatively simple descriptive model for the overall kinematic behavior that captures these features over most of the probed volume, and can be used to search for fine substructure in kinematic and metallicity space. We use this model to predict further improvements in kinematic mapping of the Galaxy expected from Gaia and LSST.

Subject headings: methods: data analysis — stars: statistics — Galaxy: halo, kinematics and dynamics, stellar content, structure

1.   Introduction

The Milky Way is a complex and dynamic structure that is constantly being shaped by the infall of matter from the Local Group and mergers with neighboring galaxies. From our vantage point inside the Milky Way disk, we have a unique opportunity to study an $\sim L^*$ spiral galaxy in great detail. By measuring and analyzing the properties of large numbers of individual stars, we can map the Milky Way in a nine-dimensional space spanned by the three spatial coordinates, three velocity components, and three stellar parameters – luminosity, effective temperature, and metallicity.

In this paper, the third in a series of related studies, we use data obtained by the Sloan Digital Sky Survey (York et al. 2000) to study in detail the distribution of tens of millions of stars in this nine-dimensional space. In Jurić et al. (2008, hereafter J08), we studied the spatial distribution of stars in the Galaxy, and in Ivezić et al. (2008, hereafter I08) we extended our analysis to include the metallicity distribution. In this paper, working with a kinematic data set unprecedented in size, we study distribution of stellar velocities. Our data include measurements from the SDSS astrometric, photometric and spectroscopic surveys: the SDSS Data Release 7 radial velocity sample includes $\sim 170,000$ main-sequence stars, and the proper motion sample includes 18.8 million stars, with about 6.8 million F/G stars for which photometric metallicity estimates are also available. These stars sample a distance range from ~ 100 pc to ~ 10 kpc, probing much further from Earth than the HIPPARCOS sample, which only covers only the nearest ~ 100 pc (e.g., Dehnen & Binney 1998; Nordström et al. 2004). With the SDSS data set, we are offered for the first time an opportunity to study *in situ* the thin/thick disk and disk/halo boundaries over a large solid angle, and using millions of stars.

In all three of the papers in this series, we have used a set of photometric parallax relations, enabled by accurate SDSS multi-color measurements, to estimate the distances to

main-sequence stars. With these distances, accurate to $\sim 10 - 15\%$, the stellar distribution in the multi-dimensional phase space can be mapped and analyzed without any additional assumptions. The primary aim of this paper is thus to develop quantitative understanding of the large-scale kinematic behavior of the disk and halo stars. From an observer's point of view, the goal is to measure and describe the radial velocity and proper motion distributions as functions of the position in, say, the r vs. $g - r$ color-magnitude diagram, and as functions of the position of the analyzed sample on the sky. From a theorist's point of view, we seek to directly quantify the behavior of the probability distribution function, $p(v_R, v_\phi, v_Z | R, \phi, Z, [Fe/H])$, where (v_ϕ, v_R, v_Z) are the three velocity components in a cylindrical coordinate system, (R, ϕ, Z) describe the position of a star in the Galaxy, and $[Fe/H]$ is its metallicity ("|" means "given").

This a different approach than that taken by the widely-used "Besançon" Galaxy model (Robin et al. 2003, and references therein), which attempts to generate model stellar distributions from "first principles" (such as initial mass function) and requires dynamical self-consistency. Instead, we simply seek to describe the directly observed distributions of kinematic quantities without imposing any additional constraints. If these distributions can be described in terms of simple functions, then one can try to understand and model those simple abstractions, rather than full voluminous data set.

As discussed in detail by J08 and I08, the disk and halo components have spatial and metallicity distributions which are well fit by simple analytic models within the volume probed by SDSS (and outside regions with strong substructure, such as Sgr dwarf tidal stream and Monoceros stream). In this paper, we develop analogous models that describe the velocity distributions of disk and halo stars.

Questions we ask include: what are the limitations of the Schwarzschild's ellipsoidal approximation (a three-dimensional gaussian distribution) for describing velocity

distribution? Given the increased distance range compared to older data sets, can we detect spatial variation of the best-fit Schwarzschild ellipsoid parameters, including its orientation? Does halo rotate on average? Is the kinematic difference between disk and halo stars as remarkable as the difference in their metallicity distributions? Do large spatial substructures, that are also traced in metallicity space, have distinctive kinematic behavior?

Of course, answers to some of these questions are known to some extent (for excellent reviews, see Gilmore et al. 1989; Majewski 1993; Helmi 2008, for context and references, see also the first two papers in this series). For example, it has been known at least since the seminal paper by Eggen et al. (1962) that high-metallicity disk stars move on nearly circular orbits, while low-metallicity halo stars move on very eccentric randomly oriented orbits. However, given the increase in the number of stars compared to previous work (orders of magnitude), increased distance limits, and accurate and diverse measurements obtained with the same facility, the previous results (see I08 for a summary of kinematic results) can be significantly improved and expanded.

The main sections of the paper include a description of the data and methodology (§2), followed by analysis of the various stellar subsamples. In §3, we begin by analyzing the proper motion sample and determining the dependence of the azimuthal (rotational) and radial velocity distributions on position for halo and disk subsamples selected along $l = 0°$ and $l = 180°$. The spectroscopic sample is used in §4 to obtain constraints for the behavior of vertical velocity component, and to measure the velocity ellipsoid tilt. The resulting model is then compared to the full proper motion sample and radial velocity samples in §5. Finally, in §6, we summarize and discuss our results, including a comparison with prior results and other work based on SDSS data (§6).

Due to length, some additional aspects of our analysis are presented separately. A detailed analysis of two-dimensional radial vs. rotational velocity distribution ($v_R - v_\phi$) for

nearby main-sequence M stars as a function of distance from the plane, Z, is presented by Kowalski et al. (in prep.). Using a sample of several million stars, they find that the $v_R - v_\phi$ distribution can be described by a sum of two Gaussians with parameters similar to those expected in the traditional thin and thick disk; however, they also find that the relative normalization of the two gaussian components does not vary by more than 0.05 from their median values of 0.65 and 0.35, as Z increases from ~ 200 pc to ~ 1.5 kpc. In contrast, using stellar counts, J08 measure a change of the thick-to-disk normalization from 0.15:0.85 to 0.65:0.35 in the same Z range. A comparison of SDSS metallicity and kinematic distributions with N-body simulations from Roškar et al. (2008) is presented in Loebman et al. (in prep). For initial results see Loebman et al. (2008). These models indicate that the unexpected absence of a velocity-metallicity correlation at the thin/thick disk boundary pointed out by I08 may be due to a combination of strong vertical age gradient and radial migration of stars. It is plausible that the same mechanism may be related to the puzzling Kowalski et al. result.

2. Data and Methodology

The characteristics of the SDSS imaging and spectroscopic data relevant to this work are described in detail in the first two papers in the series (J08, I08). Here, we briefly summarize the photometric parallax and photometric metallicity methods, and then describe the proper motion data and their error analysis. The subsample definitions are described at the end of this section.

2.1.   Photometric Parallax Method

The majority of stars in the SDSS imaging catalogs are on the main sequence (J08 and references therein) and, using the broadband colors measured by SDSS, it is possible to estimate their absolute magnitude. A maximum likelihood implementation of the photometric parallax method in the SDSS photometric system was introduced and discussed in detail in J08. The method was further refined by I08, who calibrated its dependence on metallicity using globular clusters. In addition, Sesar et al. (2008, hereafter S08) used a large sample of candidate wide binary stars to show that the expected error distribution is mildly non-gaussian, with a root-mean-square (rms) scatter of $\sim$ 0.3 mag. They also quantified biases in the derived absolute magnitudes due to unresolved binary stars.

We estimate absolute magnitudes using equation A7 in I08, which corrects for age effects, and equation A2 to account for the impact of metallicity. Based on an analysis of stars in globular clusters, I08 estimate that the probable systematic errors in absolute magnitudes determined using these relations are about 0.1 mag, corresponding to 5% systematic distance errors (in addition to the $10 - 15\%$ random distance errors).

2.2.   Photometric Metallicity

Stellar metallicity can significantly affect the position of a star in the color-magnitude diagram (there is a shift of $\sim$ 1 mag between the median halo metallicity of -1.5 and the median disk metallicity of -0.2). SDSS spectroscopy is only available for a small fraction of the stars in our sample, so we adopt a photometric metallicity method based on SDSS $u - g$ and $g - r$ colors. The relation was originally calibrated by I08 using SDSS spectroscopic metallicity. However, the calibration of SDSS spectroscopic metallicity changed at the high-metallicity end after SDSS Data Release 6. Therefore, we recalibrate

their expressions as described in the Appendix. The new calibration, given in Equation A1, is applicable to F/G stars with $0.2 < g - r < 0.6$ and has photometric metallicity errors that approximately follow a gaussian distribution with a width of 0.26 dex. In addition, the ~ 0.1 dex systematic uncertainties in SDSS spectroscopic metallicity (Beers et al. 2006; Allende Prieto et al. 2006; Lee et al. 2008; Allende Prieto et al. 2008) are inherited by the photometric metallicity estimator. We emphasize that photometric metallicity estimates are robust only in the range $-2 < [Fe/H] < 0$ (see Appendix for details).

For stars with $g - r > 0.6$, we assume a constant metallicity of $[Fe/H] = -0.7$, motivated by results for the disk metallicity distribution presented in I08 and the fact that SDSS data are too shallow to include a large fraction of red halo stars. A slightly better method would be to use disk metallicity distribution from I08 to solve for best-fit distance iteratively, but the resulting changes in the photometric distances are negligible compared to other systematic errors.

2.3.   SDSS-POSS Proper Motion Catalog

We take proper motion measurements from the Munn et al. (2004) catalog (distributed as a part of the public SDSS data releases), which is based on a comparison of astrometric measurements between SDSS and a collection of Schmidt photographic surveys. Despite the sizable random and systematic astrometric errors in the Schmidt surveys, the combination of a long baseline (~ 50 years for the POSS-I survey), and a recalibration of the photographic data using the positions of SDSS galaxies (see Munn et al. for details), result in median random proper motion errors (per component) of only ~ 3 mas yr^{-1} for $r < 18$ and ~ 5 mas yr^{-1} for $r < 20$. As shown below, systematic errors are typically an order of magnitude smaller. At a distance of 1 kpc, a random error of 3 mas yr^{-1} corresponds to a velocity error of ~ 15 km s^{-1}, which is comparable to the radial velocity accuracy

delivered by the SDSS stellar spectroscopic survey. At a distance of 7 kpc, a random error of 3 mas yr^{-1} corresponds to a velocity error of 100 km s^{-1}, which still represents a usable measurement for large samples, given that systematic errors are much smaller (~ 20 km s^{-1} at a distance of 7 kpc). The small and well-understood proper motion errors, together with a large distance limit and a large sample size (proper motion measurements are available for about 38 million stars with $r < 20$ from SDSS Data Relase 7) make this catalog an unprecedented resource for studying the kinematics of Milky Way stars.

We warn the reader that proper motion measurements publicly available prior to SDSS Data Release 7 are known to have significant systematic errors. Here we use a revised set of proper motion measurements (**?**), which are publicly available only since Data Release 7. As described in the next section, we can assess the error properties of this revised proper motion catalog using objects with known proper motion – that is, using quasars.

2.3.1. Determination of Proper Motion Errors Using Quasars

All known quasars are sufficiently far away that their proper motions are vanishingly small compared to the expected random and systematic errors in the Munn et al. catalog. The large number of spectroscopically confirmed SDSS quasars (Schneider et al. 2007) which were not used in the recalibration of POSS astrometry can therefore be used to derive robust independent estimates of these errors. In SDSS Data Release 7, there are $69,916$ quasars with $14.5 < r < 20$, redshifts in the range, $0.5 < z < 2.5$, and available proper motions (see Appendix for the SQL query used to select and download the relevant data). Within this sample of quasars, the proper motions have a standard deviation of ~ 3.1 mas yr^{-1} for each component (determined from inter-quartile range), with medians differing from zero by less than 0.2 mas yr^{-1}. The dependence of the random error on

r-band magnitude is well described by

$$\sigma_\mu = 2.7 + 2.0 \times 10^{0.4\,(r-20)}\,\mathrm{mas\ yr^{-1}} \tag{1}$$

fitting only to quasars in the range, $15 < r < 20$. When the measurements of each proper motion component are normalized by σ_μ, the resulting distribution is approximately Gaussian, with only $\sim 1.8\%$ of the quasar sample deviating by more than 3σ from zero proper motion. In addition to their dependence on magnitude, the random proper motion errors also depend on the position on the sky, but the variation is relatively small ($\sim 20\%$, see right panels in Figure 1). Finally, we find that the correlation between the errors in the two components is negligible compared to the total random and systematic errors.

The median proper motion for the full quasar sample is ~ 0.2 mas yr^{-1}, but the systematic errors can be larger by a factor of $2-3$ in small sky patches, as illustrated in Figure 1. We find that the distribution of systematic proper motion errors in ~ 100 deg^2 large patches has a width of ~ 0.67 mas yr^{-1} in each component, about twice as large as that expected from purely statistical noise (per bin, using eq. 1). As the figure shows, a few regions of the sky have coherent systematic errors at ~ 1 mas yr^{-1} (e.g. the median μ_l towards $l \sim 270°$, or μ_b towards the inner Galaxy). Therefore, the kinematics measured using proper motions in these regions should be treated with caution.

The largest systematic errors, ~ 1 mas yr^{-1} for μ_l, are seen toward $l \sim 270$ in the top left panel in Figure 1, which corresponds to $\delta \lesssim 10°$. In this region, the systematic deviation of quasar proper motions from zero is approximately parallel to lines of constant right ascension, suggesting that the data may be suffering from systematic effects due to atmospheric refraction and spectral differences between quasars and galaxies used in the recalibration of POSS astrometry. This effect would be strongest for observations obtained at high airmass, as are typical for fields at low declination (the POSS data were obtained at a latitude of $+33°$). We find that the median quasar proper motion in the δ direction is

well described by

$$\langle \mu_\delta \rangle = -0.72 + 0.019\, \delta \ \ \mathrm{mas} \ \mathrm{yr}^{-1} \tag{2}$$

for $-5° < \delta < 30°$, where δ is in degrees. At $\delta > 30°$, we find $\langle \mu_\delta \rangle \lesssim 0.2$ mas yr^{-1}.

The observed direction and magnitude of this systematic offset (corresponding to an astrometric displacement of up to ~ 30 mas) are consistent with detailed studies of atmospheric dispersion effects on observations of quasars (Kaczmarczik et al. 2007). Therefore, it is possible that the systematic errors in *stellar* proper motions (whose spectral energy distributions differ less from galaxy spectral energy distributions than is the case for quasars) are smaller than implied by Figure 1. Nevertheless, we will conservatively adopt the quasar proper motion distributions as independent estimates of systematic and random proper motion errors for stars analyzed in this work. In particular, we adopt 0.6 mas yr^{-1} as an estimate for typical systematic proper motion error.

The quasar sample has a much narrower color range than that seen in main sequence stars (96% of quasar sample satisfies $-0.2 < g - r < 0.6$), and provides a better estimate of systematic proper motion errors for blue than for red stars. Within the above well sampled color range, we find a median proper motion gradient with respect to the $g - r$ color of $\lesssim 0.1$ mas yr^{-1} mag^{-1} (per component). When the fit is extended to $g - r < 1.6$ (using a much smaller number of quasars), the gradient is still smaller than 0.5 mas yr^{-1} mag^{-1}. Hence, the proper motion systematics have a color dependence that is smaller than, or at most comparable to, their dependence on sky position.

A systematic error in proper motion of 0.6 mas yr^{-1} corresponds to a systematic velocity error of 3 km s^{-1} at 1 kpc, and ~ 20 km s^{-1} at 7 kpc. In addition, the $\sim 5\%$ systematic distance errors discussed in § 2.1 are responsible for a $\sim 5\%$ systematic velocity uncertainty. Hence, for a disk-like heliocentric tangential velocity of 20 km s^{-1}, proper motion systematics dominate at distances beyond ~ 1 kpc. Similarly, for a halo-like

heliocentric tangential velocity of 200 km s^{-1}, proper motion systematics will dominate at distances greater than 7 kpc. At smaller distances, the dominant systematic in our tangential velocity estimates comes from systematic distance errors. For most of the Galaxy volume analyzed in this work, the systematic distance errors dominate over systematic proper motion errors.

2.4.   Comparison of Proper Motions with Independent Measurements

As further tests of the proper motion errors, we have analyzed two independent sets of measurements. They confirm the results based on the analysis of quasar sample.

We have compared the SDSS-POSS proper motions to proper motion measurements by Majewski (1992) for a sample of 326 stars observed towards the North Galactic pole. Majewski's measurements have about three times smaller random errors, and comparable, but most likely, different systematic errors. The median proper motion differences between the two data sets are below 1 mas yr^{-1}, with the rms scatter $3-4$ mas yr^{-1} (per coordinate). Hence, this comparison is consistent with our error estimates discussed in the preceding section, and with Majewski's estimates.

We have also compared the SDSS-POSS proper motions with proper motions from the SDSS stripe 82 region. In Bramich et al. (2008), proper motions are computed using only SDSS data, and thus they are expected to have different, and probably smaller, systematic errors than the SDSS-POSS proper motions (random errors for the stripe 82 proper motions are larger by about a factor of 2). For $\sim$500,000 stars with both SDSS-POSS and Bramich et al. proper motion measurements, we find median differences and the rms scatter to agree with expectations. A single worrisome result is that the median difference between the two datasets is a function of magnitude: we find a gradient of 0.8 mas yr^{-1} between $r = 15$ and

$r = 20$. It is more likely that this gradient is due to systematic errors in centroiding sources on photographic plates, than a problem with SDSS data. This gradient corresponds to systematic velocity error as a function of distance, $\Delta v \sim 4$ km s^{-1} D/kpc. For example, a halo star at 5 kpc, with a relative velocity of 200 km s^{-1}, would have a systematic velocity uncertainty of 10%. This systematic error is comparable to other sources of systematic errors discussed above, and has to be taken into account when interpreting our results below.

2.5. The Main Stellar Samples

When using proper motions, random errors in the inferred velocities have a strong dependence on magnitude, and therefore distance, while systematic errors are a function of position on the sky, as discussed above. Random errors in radial velocity measurements also depend on magnitude, as fits to spectral features become more difficult at lower signal-to-noise ratios. As such, when radial velocity and proper motion measurements are analyzed simultaneously, the systematic and random errors combine in a complex way – care is needed when interpreting the results of such an analysis.

In order to minimize these difficulties, we separately analyze the proper motion sample and the much smaller sample of stars with radial velocities. Furthermore, motivated by the metallicity distribution functions presented in I08, we separately treat low-metallicity "halo" stars and high-metallicity "disk" stars. For these two samples, we require $g - r < 0.6$, the regime in which the photometric metallicity estimator is believed to be accurate. Finally, we will discuss a sample of "red" stars with $g - r > 0.6$ (roughly, $g - i > 0.8$), which are dominated by nearby (< 2 kpc) disk stars.

These samples are selected from SDSS Data Release 7 using the following common

criteria:

1. unique unresolved stationary sources: binary processing flags DEBLENDED_AS_MOVING, SATURATED, BLENDED, BRIGHT, and NODEBLEND must be false, and parameter nCHILD=0

2. the interstellar extinction in the r band, $A_r < 0.3$

3. $14.5 < r < 20$

4. high galactic latitudes: $|b| > 20°$

5. available proper motion,

yielding 20.1 million stars. The following color criteria then select stars from the main stellar locus:

- Blue stars (6.9 million):

    1. $0.2 < (g - r) < 0.6$

    2. $0.7 < (u - g) < 2.0$ and $-0.25 < (g - r) - 0.5(u - g) < 0.05$

    3. $-0.2 < 0.35(g - r) - (r - i) < 0.10$

- Red stars (11.9 million):

    1. $0.6 < (g - r) < 1.6$

    2. $-0.15 < -0.270r + 0.800i - 0.534z + 0.054 < 0.15$,

where the last condition is based on a "principal color" orthogonal to the stellar locus in the $i - z$ vs. $r - i$ color-color diagram, as defined in Ivezić et al. (2004). This condition allows for a 0.15 mag offset from the stellar locus.

During the analysis, "blue" stars are often further split by photometric metallicity (see below for more details) into candidate "halo" stars ($[Fe/H] < -1.1$) and candidate "disk" stars ($[Fe/H] > -0.9$). Subsamples with intermediate metallicities include non-negligible fractions of both halo and disk stars. Although the reduced proper motion diagram is frequently used for the separation and analysis of these two populations, we find it inadequate for our purposes. The two main reasons are that the Galaxy's vertical gradient in rotational velocity blurs the kinematic distinction between disk and halo (for a discussion, see S08), and that this method is applicable only to stars with significant proper motion (leading to severe selection effects). A detailed analysis of the performance and tradeoffs between kinematic and metallicity-based methods for disk-halo separation is presented in Bhardwaj et al. (in prep.). Although metallicities are not available for red stars, results from I08 imply that they are dominated by the disk population (red stars can only be seen out to ~ 2 kpc).

For each of the subsamples defined above, we further separate those objects with SDSS spectroscopic data (see Appendix for SQL query) into independent subsamples. In total, these spectroscopic subsamples include $172,000$ stars (out of $352,000$ stars with spectra), after an additional requirement to select only main-sequence stars; that is, stars with $\log(g) > 3.5$[1]. Of the stars with spectroscopic data, $111,000$ are blue ($0.2 < g-r < 0.6$) and $61,000$ are red ($0.6 < g-r < 1.6$). When separating low- and high-metallicity stars with spectra, we use the spectroscopic metallicity. Due to increased difficulties with measuring $[Fe/H]$ for red stars ($g-r > 0.6$) from SDSS spectra, we adopt $[Fe/H] = -0.7$ for all such stars. This value is the median spectroscopic $[Fe/H]$ for stars with $0.6 < g-r < 1.3$ ($\sigma=0.4$ dex). For over 90% of $\sim$30,000 stars with $g-r > 1.3$, $[Fe/H]$ is not successfully

---

[1]Note that the majority of stars with $g-r > 1.2$ do not have reliable measurements of $\log(g)$ – we assume that all stars with $g-r > 1.2$ are main-sequence stars.

measured (the database values are set to -9.99).

2.6. Coordinate Systems and Transformations

Following J08 and I08, we use a right-handed Cartesian galactocentric coordinate system defined by the following set of coordinate transformations:

$$X = R_\odot - D \cos(l) \cos(b)$$
$$Y = -D \sin(l) \cos(b) \tag{3}$$
$$Z = D \sin(b),$$

where $R_\odot = 8$ kpc is the adopted distance to the Galactic center, D is distance, and (l, b) are galactic coordinates. Note that the $Z = 0$ plane passes through the Sun, not the Galactic center (see J08), X axis is oriented toward $l = 180°$ and Y axis is oriented toward $l = 270°$ (the disk rotates toward $l \sim 90°$). The main reason for adopting a galactocentric coordinate system, rather than a traditional heliocentric system, is that new datasets extend far beyond the solar neighborhood.

We also use a cylindrical coordinate system defined by

$$R = \sqrt{X^2 + Y^2}$$
$$\phi = tan^{-1}\left(\frac{Y}{X}\right). \tag{4}$$

The tangential velocity, v, is obtained from the proper motion, μ, and the distance D by

$$v = 4.74 \frac{\mu}{\text{mas yr}^{-1}} \frac{D}{\text{kpc}} \text{ km s}^{-1}. \tag{5}$$

Given the line-of-sight radial velocity, v_{rad}, and two components of tangential velocity aligned with galactic coordinate system, v_l and v_b, the observed heliocentric Cartesian

velocity components are given by,

$$v_X^{obs} = -v_{rad}\cos(l)\cos(b) + v_b\cos(l)\sin(b) + v_l\sin(l)$$

$$v_Y^{obs} = -v_{rad}\sin(l)\cos(b) + v_b\sin(l)\sin(b) - v_l\cos(l) \qquad (6)$$

$$v_Z^{obs} = -v_{rad}\sin(b) + v_b\cos(b).$$

These components are related to the traditional UVW nomenclature by, $v_X = -U$, $v_Y = -V$, and $v_Z = W$, e.g., Binney & Merrifield (1998).

In order to obtain the galactocentric cylindrical velocity components, we must first correct for the solar motion. Based on HI measurements by Gunn et al. (1979), we adopt $v_{LSR} = 220$ km s^{-1} for the motion of the local standard of rest. With the adopted distance to the galactic center, $R_\odot = 8$ kpc, this value is consistent with the HIPPARCOS-based measurement by Feast & Whitelock (1997): $v_{LSR} = 218 \pm 7$ km s^{-1}. The adopted value of $R_\odot$ is motivated by geometrical measurements of the motions of stars around Sgr A*, which yield $R_\odot = 7.94 \pm 0.42$ kpc (Eisenhauer et al. 2003). For the solar peculiar motion, we adopt the HIPPARCOS result, $v_X^{\odot,pec} = -10.0 \pm 0.4$ km s^{-1}, $v_Y^{\odot,pec} = -5.3 \pm 0.6$ km s^{-1}, and $v_Z^{\odot,pec} = 7.2 \pm 0.4$ km s^{-1} (Dehnen & Binney 1998). Using these values along with Eq. 6, we obtain the galactocentric velocity components:

$$v_i = v_i^{obs} + v_i^\odot, \quad i = X, Y, Z, \qquad (7)$$

where $v_X^\odot = -10$ km s^{-1}, $v_Y^\odot = -225$ km s^{-1}, and $v_Z^\odot = 7$ km s^{-1} (note that $v_Y^\odot = -v_{LSR} + v_Y^{\odot,pec}$). Further below, we discuss attempts to directly determine the solar peculiar motion (§ 4.2) and v_{LSR} (§ 5.3) from our data.

Finally, the cylindrical components, v_R and v_ϕ, can be computed using a simple coordinate rotation,

$$v_R = v_X\frac{X}{R} + v_Y\frac{Y}{R}$$
$$v_\phi = -v_X\frac{Y}{R} + v_Y\frac{X}{R}. \qquad (8)$$

Note that for canonical prograde disk rotation $v_\phi = -220$ km s^{-1}, and for retrograde rotation $v_\phi > 0$. Stars with $v_R > 0$ move away from the Galactic center, and stars with $v_Z > 0$ move toward the north Galactic pole.

2.7. Analysis Philosophy

Such a massive data set, that extends to a large distance limit and probes a large fraction of the Galaxy volume, can be used to map stellar kinematics in great detail. It can also be used to obtain best-fit parameters of an appropriate kinematic model. However, it is not obvious what model (functional form) to chose without at least some preliminary analysis. Hence, we first discuss various projections of the multi-dimensional space of observables and obtain a number of constraints on the spatial variation of kinematics in the next two sections. We then synthesize all the constraints into a model described in § 5. Before proceeding with our analysis, we provide a brief summary of the first two papers, whose results inform the subsequent analysis.

2.8. A summary of the first two papers

Using photometric data for 50 million stars from SDSS Data Release 4, sampled over distance range from 100 pc to 15 kpc, J08 showed that the stellar number density distribution, $\rho(R, Z, \phi)$ can be well described (apart from local overdensities; the J08 best-fit was refined using residual minimization algorithms) as a sum of two cylindrically symmetric components

$$\rho(R, Z, \phi) = \rho_D(R, Z) + \rho_H(R, Z). \tag{9}$$

The disk component can be modeled as a sum of two exponential disks

$$\rho_D(R, Z) = \rho_D(R_\odot) \times$$

$$\left[\mathrm{e}^{-|Z+Z_\odot|/H_1 - (R-R_\odot)/L_1} + \epsilon_D \mathrm{e}^{-|Z+Z_\odot|/H_2 - (R-R_\odot)/L_2} \right], \tag{10}$$

and the halo component requires an oblate power-law model

$$\rho_H(R, Z) = \rho_D(R_\odot) \, \epsilon_H \left(\frac{R_\odot^2}{R^2 + (Z/q_H)^2} \right)^{n_H/2}. \tag{11}$$

The best-fit parameters are discussed in detail by J08. We have adopted the following values for parameters relevant in this work (second column in Table 10 from J08): $Z_\odot=25$ pc, $H_1 = 245$ pc, $H_2 = 743$ pc, $\epsilon_D = 0.13$, $\epsilon_H = 0.0051$, $q_H = 0.64$, and $n_H = 2.77$. The normalization $\rho_D(R_\odot)$ (essentially the local luminosity function for main sequence stars) is listed in J08 as a function of color.

Using photometric metallicity estimator for F/G main-sequence stars, I08 obtained an unbiased, three-dimensional, volume-complete metallicity distribution of $\sim$2.5 million F/G stars at heliocentric distances of up to $\sim$8 kpc. They found that the metallicity distribution functions (MDF) of the halo and disk stars are clearly distinct. The median metallicity of the disk exhibits a vertical (with respect to the Galactic plane; Z) gradient, and no gradient in the radial direction (for $Z > 0.5$ kpc and $6 < R/\mathrm{kpc} < 10$).

Similarly to stellar number density distribution, $\rho(R, Z)$, the overall behavior of the MDF $p([Fe/H]|R, Z)$ for disk stars can be well described as a sum of two components

$$p(x = [Fe/H]|R, Z, \phi) = [1 - f_H(R, Z)] \, p_D(x|Z) + f_H(R, Z) \, p_H(x), \tag{12}$$

where the halo-to-disk counts ratio is simply $f_H(R, Z) = \rho_H(R, Z)/[\rho_D(R, Z) + \rho_H(R, Z)]$.

The halo metallicity distribution, $p_H([Fe/H])$, is spatially invariant within the probed volume and well described by a Gaussian distribution centered on $[Fe/H] = -1.46$, and

with an intrinsic (corrected for measurement errors) width $\sigma_H = 0.30$ dex. For $|Z| \lesssim 10$ kpc, an upper limit on the halo radial metallicity gradient is 0.005 dex/kpc.

The disk metallicity distribution varies with Z such that its shape remains fixed, while its median, μ_D, varies as

$$\mu_D(Z) = \mu_\infty + \Delta_\mu \, \exp(-|Z|/H_\mu) \text{ dex}, \tag{13}$$

with the best-fit parameter values $H_\mu = 0.5$ kpc, $\mu_\infty = -0.82$ and $\Delta_\mu = 0.55$). The *shape* of the disk metallicity distribution can be modeled as

$$p_D(x = [Fe/H]|Z) = 0.63 \, G[x|\mu = a(Z), \sigma = 0.2] +$$
$$0.37 \, G[x|\mu = a(Z) + 0.14, \sigma = 0.2], \tag{14}$$

where the position a and the median μ_D are related via $a(Z) = \mu_D(Z) - 0.067$ (unless measurement errors are very large).

The main result of this third paper in the series is the extension of these results for number density and metallicity distributions to kinematic quantities.

3. Analysis of the Proper Motion Sample

We begin by analyzing the proper motion measurements of stars observed toward the North Galactic pole. In this region, the galactocentric azimuthal velocity, v_ϕ, and radial velocity, v_R, can be determined directly from the proper motion measurements (that is, without knowledge of the radial velocity, v_{rad}). In this way, we can study the kinematic behavior of stars as a function of metallicity and distance from the galactic plane, Z. We then extend our analysis to the entire meridional $Y = 0$ plane and study the variation of stellar kinematics with R and Z. In the following section, we only consider the northern Galactic hemisphere, where most of the proper motion data are available.

3.1. Kinematics towards the North Galactic pole

We select three stellar subsamples in the region, $b < 80$, including $14,000$ blue disk stars at $Z < 7$ kpc, $23,000$ blue halo stars at $Z < 7$ kpc, and a sample of $105,000$ red stars at $Z < 1$ kpc. In Figure 2, we plot the distribution of v_ϕ vs. v_R for $\sim 6,000$ blue disk and halo stars at $Z = 4 - 5$ kpc. In this and all subsequent two-dimensional projections of the velocity distribution we plot smoothed, color-coded maps, where the velocity distributions are estimated using the Bayesian density estimator of (Ivezić et al. 2005, see their Appendix for derivation and discussion) At a given position, the density is evaluated,

$$\rho = \frac{C}{\sum_{i=1}^{N} d_i^2}, \tag{15}$$

where d_i is the distance to the i-th neighbor in the velocity-velocity plane, and we sum over the $N = 10$ nearest neighbors. The normalization constant, C, is easily evaluated by requiring that the density summed over all pixels is equal to the total number of data points divided by the total area. The grid size is arbitrary, but the map resolution is determined by the density of points – we choose pixel size equal to one half of the mean velocity error. As shown by (Ivezić et al. 2005), this method is superior to simple Gaussian smoothing. For comparison, we also plot linearly-spaced density contours.

The six panels of Figure 2 demonstrate the variation of kinematics with metallicity, with the full range of metallicities $(-3 < [Fe/H] < 0)$ plotted in the upper left panel and subsamples with increasing metallicity running from left-to-right, top-to-bottom. The mean azimuthal velocity varies strongly with metallicity, from a non-rotating low-metallicity subsample with large velocity dispersion (top center panel) to a rotating high-metallicity sample with much smaller dispersion (bottom right panel). This strong metallicity-kinematic correlation is qualitatively the same as discussed in the seminal paper by Eggen et al. (1962), except that here it is reproduced *in situ* with a $\sim$100 times larger nearly-complete sample, thus extending it beyond the solar neighborhood. There are some indications of

substructure in the velocity distribution, but much of it remains unresolved due to the large velocity measurement errors.

The substructure becomes more apparent in Figure 3, where we plot the same velocity-space projection for $60,000$ stars within $Z < 2.5$ kpc. In this figure, the panels show subsamples of increasing distance from the galactic plane, beginning with $Z = 0.1 - 0.2$ kpc in the upper left panel (note the changing axes between the top and bottom rows). The substructure seen in the closest bin probed by red stars is very similar to the substructure seen in the local HIPPARCOS sample (Dehnen 1998). Note that unlike Dehnen's result, which was based on maximum likelihood analysis over the entire sky, our map is a direct mapping of the velocity distribution of stars selected from a small region (~ 300 deg^2). Using a subsample of $\sim 17,000$ HIPPARCOS stars with full three-dimensional velocity information, Nordström et al. (2004) have detected the same kinematic morphology. The similarity between these HIPPARCOS-based and our velocity distributions, including the multi-modal behavior reminiscent of Eggen's groups (Eggen 1996), is encouraging given the vastly different data sources. The similarity of observed substructure with Eggen's groups is even more striking for stars from a closer distance bin ($Z = 50 - 100$ pc) that is matched to distances probed by the HIPPARCOS sample, see Figure 4. As suggested by De Simone, Wu & Tremaine (2004), these moving groups arise from irregularities in the Galactic potential.

The remainder of our analysis will focus on blue stars, which sample a much larger distance range. For a detailed study of the velocity distribution of nearby red stars, including a discussion of non-gaussianity, vertex deviation and difficulties with traditional thin/thick disk separation, we refer the reader to Kowalski et al. (in prep.).

The dependence of the rotational velocity on height above the galactic plane is shown in Figure 5. The two subsamples display remarkably different kinematic behavior (first

seen locally by Eggen et al. 1962) with halo stars exhibiting a small constant rotational motion (~ -20 km s^{-1}), and the disk stars exhibiting a large rotational velocity component (~ -200 km s^{-1} at $Z \sim 1$ kpc) that decreases with height above the galactic plane.

We have performed the same analysis using proper motions based only on POSS data, with SDSS positions not included in the proper motion fit (not publicly available). While random proper motion errors become larger when SDSS data are not used, the median rotational velocity for halo stars decreases to only 5 km s^{-1}, suggesting that the apparent rotational motion in the halo subsample is caused by systematic errors. These tests also suggest that the leading contribution to systematic proper motion errors could be a difference between SDSS (digital data) and POSS (digitized photographic data) centroiding algorithms. In addition, Smith et al. (2009) did not detect halo rotation using a smaller sample but with more robust proper motion measurements based on only SDSS data). We conclude that the net halo rotation in the direction of the north galactic pole is $|v_{rot}| \lesssim 10$ km s^{-1}. In addition, the measured halo velocity dispersion increases with Z, but when random measurement errors are taken into account, the data are consistent with a constant dispersion of $\sigma_\phi^H = 85 \pm 5$ km s^{-1} (derived using test described in § 5).

The decrease of rotational velocity with Z for disk stars (sometimes called asymmetric drift, velocity lag, or velocity shear; see section 3.4 of I08 for more details and references to related work) is in agreement with a preliminary analysis presented in I08. We find that the observed behavior in the $Z = 1 - 4$ kpc range can be described by

$$\langle v_\phi \rangle = -205 + 19.2\,|Z/\mathrm{kpc}|^{1.25}\ \mathrm{km\ s}^{-1}. \tag{16}$$

The measured rotational velocity dispersion of disk stars increases with Z faster than can be attributed to measurement errors. Using a functional form $\sigma = a + b|Z|^c$, we fit an *intrinsic* velocity dispersion of

$$\sigma_\phi^D = 30 + 3.0\,|Z/\mathrm{kpc}|^{2.0}\ \mathrm{km\ s}^{-1}. \tag{17}$$

This function and the best-fit halo rotational velocity are shown as a dotted lines in the bottom right panel of Figure 5 (see Table 1 for a summary of all best-fit parameters). I08 fit a linear model to v_ϕ vs. Z, but the difference between this result and their equation 15 never exceeds 5 km s^{-1} for $Z < 3$ kpc. The errors on the power-law exponents of Equations 16 and 17 are ~ 0.1 and ~ 0.2.

However, a description of the velocity distribution based solely on the first and second moments (Equations 16 and 17) does not fully capture detailed behavior of our data. As already discussed by I08, the rotational velocity distribution for disk stars is strongly non-gaussian (see their figure 13). It can be formally described by a sum of two gaussians with a fixed normalization ratio and a fixed offset of their mean values

$$p_D(x = v_\phi|Z) = 0.75\, G[x|v_n(Z), \sigma_1] +$$
$$0.25\, G[x|v_n(Z) - 34\,\mathrm{km\ s^{-1}}, \sigma_2], \tag{18}$$

where

$$v_n(Z) = -194 + 19.2\, |Z/\mathrm{kpc}|^{1.25}\ \mathrm{km\ s^{-1}}. \tag{19}$$

for $|Z| < 5$ kpc.

The intrinsic velocity dispersions, σ_1 and σ_2, are modeled as $a + b|Z|^c$, with best-fit parameters listed in Table 1 (see σ_ϕ^1 and σ_ϕ^2). Closer to the plane, in the $0.1 < Z < 2$ kpc range probed by red stars, the median rotational velocity and velocity dispersion are consistent with extrapolation of fits derived here using much more luminous blue stars.

Figure 6 shows the v_ϕ distribution for four bins in Z (analogous to figure 13 from I08), overlaying two-component gaussian fits with the measurement errors and $v_n(Z)$ as free parameters. The mean velocity and velocity dispersion exhibit ~ 10 km s^{-1} variations relative to their expected values; while such deviations could be evidence of kinematic substructure, they are also consistent with the plausible systematic errors. We conclude that

Equations 18 and 19 provide a good description of the disk kinematics for stars observed toward the North Galactic Pole, withing the limitations set by random and systematic errors in our dataset.

The dependence of the galactocentric radial velocity on Z is plotted for halo and disk subsamples in Figure 7. The median values (bottom left panel) are consistent with zero within the plausible systematic errors $(10 - 20$ km s$^{-1})$ at all Z. The intrinsic dispersion for halo stars is consistent with a constant value of $\sigma_R^H = 135 \pm 5$ km s^{-1}. For disk stars, the best-fit functional form $\sigma = a + b|Z|^c$ is

$$\sigma_R^D = 40 + 5\,|Z/\mathrm{kpc}|^{1.5} \ \mathrm{km} \ \mathrm{s}^{-1}. \tag{20}$$

The σ_R^D/σ_ϕ^D ratio has a constant value of ~ 1.35 for $Z < 1.5$ kpc, and decreases steadily at larger Z to 1 at $Z \sim 4$ kpc.

3.2. Kinematics in the Meridional $Y \sim 0$ Plane

The analysis of the rotational velocity component can be extended to the meridional plane defined by $Y = 0$, on which the longitudinal proper motion depends only on the rotational velocity component and latitudinal proper motion, v_b, is a linear combination of radial and vertical components,

$$v_b = \sin(b)v_R + \cos(b)v_Z. \tag{21}$$

Figure 8 plots v_ϕ and v_b as functions of R and Z for halo and disk stars within $10°$ of the meridional plane. The median v_b is close to zero throughout most of the plotted region, as would be expected if the median v_R and v_Z are zero (the behavior of v_Z is discussed in the next section). One exception is a narrow feature with $v_b \sim -100$ km s^{-1} for $R < 4$ kpc. While a cold stellar stream would produce such a signature, its narrow geometry points

directly at the observer. This behavior is also consistent with a localized systematic proper motion error. Indeed, the bottom left panel in Figure 1 shows that the systematic latitudinal proper motion error at $l \sim 0$, $b \sim 45°$ is about 1 mas yr^{-1}, corresponding to a velocity error of ~ 100 km s^{-1} at a distance of 7 kpc.

As seen in the upper left panel of Figure 8, the median v_ϕ for halo stars is close to zero for $R < 12$ kpc. In the region with $R > 12$ kpc and $Z < 6$ kpc, the median indicates surprising prograde rotation in excess of 100 km s^{-1}. This behavior is also seen in disk stars and is likely due to Monoceros stream, which has a metallicity intermediate between disk and halo stars and rotates faster than disk stars (see sections 3.5.1 and 3.5.2 in I08). There is also an indication of localized retrograde rotation for halo stars with $Z =\sim 9$ kpc and $R \sim 15$ kpc (corresponding to $l \sim 180°$, $b \sim 50°$, and a distance of ~ 11 kpc). Stars with $Z = 8 - 10$ kpc and $R = 15 - 17$ kpc have median v_ϕ larger by 40 km s^{-1} ($\sim 1\sigma$ effect) and median $[Fe/H]$ larger by 0.1 dex ($\sim 5\sigma$ effect) than stars with $Z = 8 - 10$ kpc and $R = 7 - 13$ kpc. A systematic error in μ_l of ~ 0.8 mas yr^{-1} is required to explain this kinematic feature as a data problem (though this would not explain the metallicity offset). However, the top right panel in Figure 1 shows that the systematic μ_l errors in this sky region are below 0.5 mas yr^{-1}, so this feature may be real. We note that in roughly the same sky region and at roughly the same distance, Grillmair & Dionatos (2006) have detected a narrow stellar stream.

In order to visualize the extent of "contamination" by Monoceros stream, we replace the rotational velocity for each disk star by a simulated value drawn from distribution described by Equation 18. We subtract this model from the data and the residuals are shown in the right panel of Figure 9. The position of the largest deviation is in excellent agreement with the position of Monoceros stream quantified in I08 ($R \sim 3$ kpc and $|Z| \sim 3 - 4$ kpc). Further evidence for the presence of Monoceros stream is shown in Figure 10), in which we analyze

v_ϕ vs. $[Fe/H]$ as a function of R for blue stars at $Z = 4 - 6$ kpc. As evident in the bottom right panel, there is a significant excess of stars at $R > 17$ kpc with $-1.5 < [Fe/H] < -0.5$ which rotate with ~ 200 km s^{-1}.

4.   Analysis of the Spectroscopic Sample

Despite its smaller size, the SDSS spectroscopic sample of $\sim 100,000$ main-sequence stars is invaluable because it enables a direct[2] study of the three-dimensional velocity distribution. The sample extends to a distance of $\lesssim 10$ kpc, at which it can deliver velocity errors as small ~ 10 km s^{-1} (corresponding tangential velocity errors are ~ 150 km s^{-1} at a distance of 10 kpc). For each object in the SDSS spectroscopic survey, its spectral type, radial velocity, and radial velocity error are determined by matching the measured spectrum to a set of stellar templates, which were calibrated using the ELODIE stellar library. Random errors on the radial velocity measurements are a strong function of spectral type and signal-to-noise ratio, but are usually < 5 km s^{-1} for stars brighter than $g \sim 18$, rising sharply to ~ 15 km s^{-1} for stars with $r = 20$. We model the behavior of the radial velocity errors as

$$\sigma_{rad} = 3 + 12 \times 10^{0.4\,(r-20)} \quad \text{km s}^{-1}. \tag{22}$$

We begin our analysis with blue disk and halo stars, and then briefly discuss the kinematics of nearby red M stars.

---

[2]Statistical deprojection methods, such as that recently applied to a subsample of M stars discussed here by Fuchs et al. (2009) can be used to indirectly infer the three-dimensional kinematics.

4.1. Velocity Distribution

We select $42,000$ stars with $0.2 < g - r < 0.6$ ($29,000$ have $b > 20°$) and, using spectroscopic metallicity, we separate them into $28,500$ candidate halo stars with $[Fe/H] < -1.1$, and $\sim 10,000$ disk stars with $[Fe/H] > -0.9$. Assuming the spectroscopic metallicities accurately separate disk from halo stars, we estimate that a photometric metallicity cut to the same sample would have a 14% contamination rate.

The dependence of the median vertical velocity (v_z) and its dispersion on height above the disk is plotted in Figure 11 for halo and disk subsamples. The median values of v_Z are consistent with zero to better than 10 km s^{-1} at $Z < 5$ kpc, where statistical fluctuations are small.

As with σ_ϕ and σ_R, the vertical velocity dispersion can be modeled using a constant dispersion for halo stars ($\sigma_Z^H = 85$ km s^{-1}), while for disk stars, the best-fit functional form is

$$\sigma_Z^D = 25 + 4\,|Z/\text{kpc}|^{1.5} \ \text{km s}^{-1}. \tag{23}$$

The other two velocity components behave in a manner consistent with Equations 16, 17, and 20, just as they did in the proper motion sample. This is encouraging because the spectroscopic sample is collected over the entire northern hemisphere, unlike the proper motion subsample studied in § 3.1, which is limited to $b > 80°$.

The availability of all three velocity components in the spectroscopic sample makes it possible to study the orientation of velocity ellipsoid. Figure 12 shows the two-dimensional projections of the velocity distribution for subsamples of candidate halo stars with $0.2 < g - r < 0.4$. The top row corresponds to stars above the Galactic Plane at $3 < Z/\text{kpc} < 4$, while the bottom row is for stars the same distance below the plane. The velocity ellipsoid is clearly tilted in top and bottom left panels, with a tilt angle consistent

with $v_Z/v_R = R/z$. While the tilt angle errors are too large to obtain an improvement over existing measurements of $R_\odot$, it is remarkable that the northern and southern subsamples agree so well[3]. In addition, when the $Z = 3 - 5$ kpc sample is divided into three subsamples with $7 < R < 11$ kpc, the tilt angle varies by the expected $\sim 8°$ in correct direction (see Figure 13). For all bins in the $R - Z$ plane, the best fit tilt angle is statistically consistent (within $5°$) with $v_Z/v_R = R/z$. The other two projections of the velocity distribution for halo stars do not show significant tilt to within $\sim 3°$.

If we transform the velocities to a spherical coordinate system,

$$v_r = v_R \frac{R}{R_{\mathrm{gc}}} + v_Z \frac{Z}{R_{\mathrm{gc}}}$$
$$v_\theta = v_R \frac{Z}{R_{\mathrm{gc}}} - v_Z \frac{R}{R_{\mathrm{gc}}}, \tag{24}$$

where $r = R_{gc} = (R^2 + Z^2)^{1/2}$ is spherical galactocentric radius, we find no statistically significant tilt in any of the two-dimensional velocity-space projections for halo stars (with tilt angle errors ranging from $\sim 1°$ to $\sim 5°$).

As shown in Figure 14, we see no evidence for a velocity ellipsoid tilt in v_Z vs. v_R for the disk stars. The plotted subsamples are again selected to have colors, $0.2 < g - r < 0.4$, but are selected closer to the Galactic Plane, $|Z| = 1.5 - 2.5$ kpc, in order to improve statistics and reduce contamination from halo stars. The velocity ellipsoid tilt is consistent with zero within $\sim 1\sigma$ and alignment of the velocity ellipsoid with the spherical coordinate system of Equation 24 is ruled out at a $\sim 2\sigma$ or greater confidence level for each of five analyzed $R - Z$ bins ($R = 6 - 11$ kpc, with $\Delta R = 1$ kpc). We conclude that there is no evidence for a velocity ellipsoid tilt in the disk subsample, but caution that, due to the

---

[3]A plausible, if somewhat optimistic, tilt angle uncertainty of $1°$ corresponds to $R_\odot$ error of 0.5 kpc; extending the sample to $|Z| = 8$ kpc could deliver errors of 0.3 kpc per bin of a similar size.

small Z range, the data cannot easily distinguish cylindrical and spherical alignment.

Vertex deviation is analogous to the velocity ellipsoid tilt discussed above, but is defined in the v_ϕ vs. v_R plane instead of the v_Z vs. v_R plane. The same plots for red $(g - r > 0.6,$ median 1.2$)$ disk stars are shown in the center top and bottom panels in Figure 15. These stars can be traced closer to the plane, $|Z| = 0.6 - 0.8$ kpc, and in both hemispheres, the data are consistent with a vertex deviation of $\sim 20°$, with an uncertainty of $\sim 10°$. This result is consistent with the vertex deviation obtained by Fuchs et al. (2009).

Another interpretation for the v_ϕ vs. v_R distribution of disk stars invokes a two-component velocity distribution, which can result in a similar deviation even if each component is perfectly symmetric in the cylindrical coordinate system. Kowalski et al. (in prep.) find that the v_ϕ vs. v_R distribution for red stars toward the North Galactic Pole, with $0.1 < Z/\mathrm{kpc} < 1.5$, can be fit by a sum of two gaussian distributions that are offset from each other by ~ 10 km s^{-1} in each direction. This offset results in a non-zero vertex deviation if the sample is not large enough, or measurements are not accurate enough, to resolve the two gaussian components. This double-gaussian structure would be at odds with the classical description based on the Schwarzschild approximation – we refer the interested reader to the Kowalski et al. study for more details. Unfortunately, the spectroscopic samples are not large enough to distinguish a two-component model from the standard interpretation.

4.2. Direct determination of the solar peculiar motion

If there is no net streaming motion in the Z direction in the solar neighborhood, the median heliocentric v_Z^{obs} for nearby stars should be equal to $v_Z^{\odot}$ (7 km s^{-1}, based on an analysis of HIPPARCOS results by Dehnen & Binney 1998). We do not expect a large

velocity gradient within ~ 1 kpc from the sun, so we select from the spectroscopic sample $\sim 13,000$ M dwarfs with $2.3 < g - i < 2.8$. In the northern hemisphere, we have $5,700$ stars with a median heliocentric velocity, $\langle v_Z^{\mathrm{obs}} \rangle = -1.8$ km s^{-1}, while for stars in the southern hemisphere we get $\langle v_Z^{\mathrm{obs}} \rangle = -11.0$ km s^{-1}. This difference is likely due to a systematic radial velocity error. If we simultaneously vary an assumed radial velocity error, Δ_{rad}, and the solar peculiar motion, $v_Z^\odot$, while requiring that the median v_Z^{obs} should be the same for both hemispheres, we obtain $\Delta_{\mathrm{rad}} = 5.0 \pm 0.4$ km s^{-1} and $v_Z^\odot = 6.5 \pm 0.4$ km s^{-1}. This value for $v_Z^\odot$ is in excellent agreement with the HIPPARCOS value of 7.2 ± 0.4 km s^{-1} (Dehnen & Binney 1998). This systematic offset in SDSS radial velocities is probably due to the small number of ELODIE templates for red stars. A similar analysis for blue stars does not yield a robust detection of the velocity offset. A detailed comparison of SDSS radial velocities with radial velocity standards from the literature arrived at the same null result for blue stars.

As with the vertical component of the solar peculiar motion, if the adopted value of $v_X^\odot = -10$ km s^{-1} were incorrect, the median v_R would deviate from zero. The variance of the median v_R for samples of nearby M stars (subselected by distance and color) is 0.5 km s^{-1}, which is an upper limit on the error in the adopted value of $v_X^\odot$. This result, which is based on the full three-dimensional velocity distribution, agrees well with results from indirect statistical deprojection methods using only proper motions (Dehnen 1998; Fuchs et al. 2009).

For both blue and red disk stars, the extrapolation of the median v_ϕ to $Z = 0$ gives -205 km s^{-1}. Since we corrected stellar velocities for an assumed solar motion of -225 km s^{-1}, this implies that the Y component of the Sun's velocity relative to the bulk motion of stars in the solar neighborhood is 20 km s^{-1}, in agreement with the recent results obtained by Fuchs et al. (2009) for the same data set. A similar value was obtained by

Dehnen & Binney (1998) for their[4] subsample of red stars within 100 pc.

5.   A Model for Kinematics of Disk and Halo Stars

Informed by the results from the preceding two sections, here we introduce a model that aims to describe the global behavior of stellar kinematics. In our model, we do not attempt to account for kinematic substructure (e.g., Monoceros stream) or the bulge region, nor do we incorporate any complex kinematic behavior close to the galactic plane. Nevertheless, we attempt to capture the gross properties of the data in the volume probed by SDSS, including the bulk kinematic trends and the kinematic differences between high-metallicity disk stars and low-metallicity halo stars. We describe the model in § 5.1, and then in § 5.2 we test it using both the proper motion and radial velocity samples.

5.1.   Kinematic Model

For halos stars, a single velocity ellipsoid (expressed in a Galactocentric spherical coordinate system, see § 4.1) is a good description of the gross halo kinematics within the 10 kpc distance limit of our sample. Our model assumes that the halo has no net rotation (see below for a test of this assumption), and that the principal axes of the velocity ellipsoid are aligned with spherical coordinate system. The velocity dispersions measured in § 3 and § 4, $\sigma_R^H = 135$ km s^{-1}, $\sigma_\phi^H = 85$ km s^{-1}, and $\sigma_Z^H = 85$ km s^{-1}, are expressed in a cylindrical coordinate system. The interplay between proper motion, radial velocity and distance

---

[4]They extrapolated the mean azimuthal motion of color-selected samples, which is correlated with the radial velocity dispersion, to zero dispersion and obtained $v_Y^{\odot,pec} = -5.3$ km s^{-1}, used here.

measurement errors is complex, so we use Monte Carlo simulations to translate them to spherical coordinates. Doing this, we obtain $\sigma_r^H = 141$ km s^{-1} and $\sigma_\theta^H = 75$ km s^{-1} (σ_ϕ^H is unchanged), with uncertainties of ~ 5 km s^{-1}.

For disk stars within $\sim 1 - 2$ kpc from the Sun, the velocity measurement errors are sufficiently small and samples are sufficiently large to resolve rich kinematic substructure (e.g., see Figure 3). This behavior is quantified in detail in Kowalski et al. (in preparation), but here we simply use the two-component model given by eqs. 18 and 19 to describe the non-gaussian v_ϕ distribution and velocity shear seen for disk stars. Furthermore, we assume that v_R and v_Z have uncorrelated gaussian distributions with zero mean and Z-dependent intrinsic dispersion parameters listed in Table 1. As discussed in section 4, there is no compelling evidence for a tilt in the velocity ellipsoid of blue stars in the $v_R - v_Z$ plane, so we model the disk velocity ellipsoid in cylindrical coordinates.

5.2. Global Model Tests

Our model predicts distributions of the three measured kinematic quantities, v_{rad}, μ_l and μ_b, for an arbitrary control volume defined by color, magnitude, and sky coordinates. We can test the consistency of this model with our data by computing the residuals of each kinematic quantity,

$$\chi = \frac{d - m}{(\sigma_d^2 + \sigma_m^2)^{1/2}}, \tag{25}$$

where σ_d is the measurement error of the data and σ_m is the dispersion predicted by the model. For all three kinematic quantities, we find $\bar{\chi} \simeq 0$ to within 0.05 for all three quantities, with dispersions of $\sim 1.05 - 1.1$. While this result is a necessary condition for the model to be acceptable, it is not sufficient. A stronger test of the model was shown in Figure 9 for disk stars, but in what follows, we perform additional tests that cover all sky regions with available data.

5.2.1. Tests With the Radial Velocity Sample

Figure 16 compares the medians and dispersions for measured and modeled radial velocities of halo stars. The alignment of the velocity ellipsoid with spherical galactocentric radius is clearly seen in the bottom left panel, where the data show a dispersion gradient moving away from the Galactic Center. The increased dispersion towards $l = 180$ was misinterpreted by Ivezić et al. (2006) to be a sign of substructure. There are no large discrepancies between the measured and predicted behavior – the median value of the difference between observed and modeled values is 4.6 km s^{-1}, with a scatter of 19 km s^{-1} (see top right panel). A similar scatter is obtained between two model realizations with the same number of stars and measurement errors. The dispersion ratio, $\sigma^d_{\mathrm{rad}}/\sigma^m_{\mathrm{rad}}$, is centered on 1.13, with a scatter of 0.2 (see bottom right panel). For pairs of model realizations, the ratio is always centered on one to within 0.02, with a scatter of 0.2, suggesting that the observed velocity dispersion is about 10% larger than predicted by our smooth model. If the residuals were due to halo rotation, we would expect a spatial coherence. Similarly, for disk stars at $1 < d < 2.5$ kpc, the median radial velocity residual is 2.8 km s^{-1}, with a scatter of 6.6 km s^{-1} (not shown).

5.2.2. Tests Based on Proper Motion Sample

The large size of the proper motion sample enables a much higher spatial resolution when searching for structure in the model residuals. We have compared observed and modeled proper motion distributions in narrow bins of distance, across the sky, and separately for disk and halo subsamples. As an illustration, Figures 17 and 18 show the median longitudinal and latitudinal proper motion observed for disk stars. There is very little change in the proper motion distribution among different distance bins because of the nearly linear vertical rotational velocity gradient. The residuals for longitudinal proper

motion are shown in Figure 19. They provide weak evidence for either substructure or a radial gradient that is not modeled, but it is difficult to distinguish these two possibilities with these data alone.

A comparison of disk and halo subsamples in a distance bin centered on $d = 4$ kpc is shown in Figure 20. The largest data vs. model discrepancy for halo stars, seen in the bottom left panel towards $l \sim 0°$, is also seen from a different viewing angle in the top left panel of Figure 8 ($R \sim 6$ kpc and $Z \sim 2$ kpc). It is likely that this discrepancy is due to contamination of halo sample by disk stars. Figure 21 shows the residuals for halo stars selected from the $8 - 10$ kpc distance bin. The residuals for both proper motion components show similar morphology to the systematic proper motion errors plotted in the two left panels of Figure 1. In this distance bin, they correspond to velocity errors of ~ 30 km s^{-1}; as such, kinematic substructure in the halo will be difficult to discern with this sample at $\gtrsim 10$ kpc. We note that it is tempting to associate the coherent μ_l residuals towards $l \sim 300°$ and $l \sim 60°$ with the Virgo overdensity (see J08). However, the top left panel in Figure 1 clearly shows systematic proper motion errors of the required amplitude (~ 1.5 mas yr^{-1}) in the same sky region.

Schlaufman et al. (2009, in preparation) use SDSS radial velocity data measurements of metal-poor turnoff stars to search for cold streams (which they term ECHOs). In 137 lines of sight, they detect ten ECHOs. The six northern ECHOs from their table 2 (class I peak detections) are shown as white circles in the bottom two panels of Figure 21. It seems plausible that four of these ECHOs might be associated with Monoceros stream ($b \sim 30°$), while one of the two remaining detections (at $l = 162.4°$ and $l = 59.2°$) is associated with the Grillmair & Dionatos (2006) stream. The ECHO at $l = 100.7°$ and $b = 56.8°$ remains unassociated with any known substructure.

We conclude that our model reproduces the first and second moments of the velocity

distributions reasonably well for both disk and halo stars. Except in the region close to Monoceros stream, the non-gaussian v_ϕ distribution for disk stars is also well described. On average, the model agrees with the data to within ~ 1 mas yr^{-1} for proper motions, ~ 10 km s^{-1} for radial velocities.

5.3. Constraints on v_{LSR} from Large-Scale Halo Kinematics

The proper motion distribution for halo stars towards the Galactic poles depends only on the difference between the velocity of the local standard of rest (given that the solar peculiar motion is known to ~ 1 km s^{-1}), v_{LSR}, and v_ϕ for halo stars. At least in principle, samples that extend over a large sky area can be used to provide constraints on both the halo rotation and v_{LSR}. Figure 22 compares the radial velocity and longitudinal proper motion residuals between two models with $(v_\phi^{\mathrm{halo}}, v_{LSR}) = (-20, 180)$ km s^{-1}, and $(20, 220)$ km s^{-1} (for both we fixed $v_{\mathrm{LSR}} - v_\phi^{\mathrm{halo}} = 200$ km s^{-1}, to make the models agree with the data towards the North Galactic pole, see Figure 5). In order to distinguish these two models observationally, systematic errors in the radial velocities must be below 10 km s^{-1}, and systematic errors in the observed proper motions must be below 1 mas yr^{-1}. These requirements are comparable to the systematic errors in our data set, so we can only state that the data are consistent with $v_{LSR} \sim 200$ km s^{-1} (or similarly, no halo rotation) to an accuracy of ~ 20 km s^{-1}. The proper motion measurements from the Gaia survey (Perryman et al. 2001) will be sufficiently accurate to exploit the full potential of this method.

5.4.   Kinematic Parallax Relation

Any constraint on our best-fit model parameters that uses proper motions is sensitive to the systematic errors in the distance scale obtained from our photometric parallax relationship. However, since our model is a good fit to the radial velocity data alone (see Figure 16), it is possible to estimate distance errors by minimizing the differences between the observed and modeled proper motion distributions. Such a kinematic parallax relation, derived from a combination of radial velocity and proper motion data sets, was proposed for the solar neighborhood by Binney & Tremaine (2008). Unlike in the solar neighborhood, our volume is sufficiently large that kinematics vary with position. Nevertheless, it is conceptually the same method; a dipole (in our case a more complex angular function) is fit to the radial velocity and proper motion distributions and the ratio of the best-fit dipole magnitudes constrains the distance scale.

Using only low-metallicity halo stars, we obtain a distance scale error of $\sim 5\%$ – our adopted absolute magnitudes should be ~ 0.1 mag brighter. This offset is consistent with expected systematic errors in the calibration of photometric parallax relation (see J08). In other words, the adopted distance scale properly connects the radial and proper motion distributions. This method provides much weaker distance scale constraints for disk stars than for halo stars because the disk's vertical velocity gradient leads to a degeneracy between errors in the distance scale and errors in the adopted disk velocity. The radial velocity measurements do not constrain the velocity scale because the reference point depends on distance.

6.   Summary and Discussion

This is the first analysis based on SDSS data that simultaneously studies the kinematics of halo and disk populations. Past studies of halo stars alone were performed by Carollo et al. (2007) and Smith et al. (2009), while disk samples ranging from nearby M stars to distant F/G stars have been studied by Bochanski et al. (2007) and Fuchs et al. (2009). Throughout this paper, we have quantified the probability distribution function $p_3(\mu_l, \mu_b, v_{rad}|u - g, g, g - r, l, b)$, introduced in I08, that describes proper motion and radial velocity measurements in the g vs. $g - r$ color-magnitude diagram as a function of position on the sky and $u - g$ color. We have developed a simple empirical model with disk and halo components that map well to populations detected in the stellar density distribution (J08) and the metallicity distribution (I08). At distances accessible to the HIPPARCOS survey (< 100 pc), we obtain encouraging agreement with results from Dehnen & Binney (1998), Dehnen (1998), and Nordström et al. (2004). The extension of kinematic mapping to distances up to ~ 10 kpc with millions of stars represents significant observational breakthrough and delivers powerful new constraints on dynamical structure of the Galaxy. In less then two decades, the observational material for such *in situ* mapping has progressed from first pioneering studies based on only a few hundred objects (Majewski 1992) to the massive dataset discussed here.

6.1.   Disk Kinematics

The Galaxy's disk kinematics are dominated by rotation with a smooth vertical gradient. Our analysis extends the early measurements of this gradient (e.g., Murray 1986; Majewski 1992) to vastly larger sky area and to a much larger distance range. The mean rotational velocity and the three velocity dispersions for disk stars can be modeled as simple functions of the form $a + b|Z|^c$ (see Equations 18 and 19, and Table 1). The rotational

velocity distribution for the disk component is non-gaussian and can be formally modeled as a sum of two gaussian components with fixed normalization ratio for $|Z| \gtrsim 1$ kpc. The fact that the normalization ratio of these two components does not vary with Z is at odds with the standard disk decomposition into thin and thick disk components (see also sections 3.4.4 and 4.2.1 in I08). Based on N-body simulations performed by Roškar et al. (2008), Loebman et al. (2008) argued that the absence of a velocity-metallicity correlation at the thin/thick disk boundary, pointed out by I08, may be due to a combination of a strong vertical age gradient and radial migration of stars. A more detailed study will be presented in Loebman et al. (in preparation). A significant vertical age gradient for disk stars is also supported by an analysis of active M dwarfs presented in Bochanski et al. (2007). Such an age gradient, together with the measured dispersion–age correlations for disk stars (e.g., Nordström et al. 2004; Rocha-Pinto et al. 2004, may be responsible for the measured increase of velocity dispersions with distance from the Galactic plane.

Close to the plane, the proper motion data imply a complex multi-modal velocity distribution which is inconsistent with a description based on a simple Schwarzschild ellipsoid. It is reassuring that we obtained a velocity distribution morphology very similar to that obtained by Dehnen (1998) using statistical deprojection of the HIPPARCOS data, and directly by Nordström et al. (2004) using a subsample of HIPPARCOS stars with full three-dimensional velocity information. In addition, our results for the first and second moments of the velocity distribution for nearby M stars agree with analogous results obtained recently by Fuchs et al. (2009). The orientation of the velocity ellipsoid is strongly affected by multi-modal structure, so one should take care in its interpretation. We discuss these issues in more detail in Kowalski et al. (in preparation).

6.2. Halo Kinematics

Our results for the velocity distribution of halo stars are in excellent agreement with Smith et al. (2009). They used proper motion measurements that are based only on SDSS data, and thus have significantly different, and most likely much smaller, systematic errors than the SDSS-POSS proper motion measurements analyzed here. The larger size of the Munn et al. (2004) catalog allows us to rule out the possibility that the Smith et al. result was biased by local substructure. The close agreement of our results for the orientation and size of the halo velocity ellipsoid (we obtained $\sigma_r^H = 141$ km s^{-1}, $\sigma_\theta^H = 75$ km s^{-1}, and $\sigma_\phi^H = 85$ km s^{-1}, and their values are 142 km s^{-1}, 77 km s^{-1}, and 81 km s^{-1}, respectively) are encouraging. Their estimated errors of 2 km s^{-1} apparently do not include systematic effects (such as errors in photometric parallax; both studies used the same calibration from I08) – based on our Monte Carlo simulations, we believe that true errors cannot be smaller than ~ 5 km s^{-1}. Additional evidence for the tilt of the velocity ellipsoid comes from the RAVE survey (Siebert et al. 2008). The measurement of the velocity ellipsoid for halo stars represents a strong constraint for the shape of gravitational potential, as discussed by Smith et al. (2009).

We note that (Majewski 1992) measured a retrograde halo rotation using stars observed towards the North Galactic pole (in our nomenclature, he obtained a mean rotational velocity $v_\Phi = 50 \pm 16$ km s^{-1}). A star-by-star comparison of his data and the data analyzed here showed that photometric and proper motion measurements agree within the stated errors. The main reason for different conclusions about halo rotation are different distance scales: his distances are on average 30% larger than our distances, resulting in overestimated tangential velocities.

The kinematic measurements for halo stars presented here should not be extrapolated beyond the sample distance limit of 10 kpc. For example, using 241 halo objects, including

stars, globular clusters, and satellite galaxies, Battaglia et al. (2005) detected a continuous decline of the radial velocity dispersion beyond a galactocentric radius of ~ 30 kpc, from about 120 km s^{-1} to 50 km s^{-1} at ~ 120 kpc. In addition, the distance limit of our sample, together with the increasing insensitivity of photometric metallicity indicator for $[Fe/H] < -2.5$, prevent us from robustly testing the possible halo dichotomy discussed by Carollo et al. (2007).

6.3. Kinematic Substructure

The model developed here can be used to search for kinematic substructure with a low contrast level. For example, Schlaufman et al. (2009, in preparation) had to generate a background model when searching for cold streams using radial velocity data; a similar study for the solar neighborhood was performed by Klement et al. (2009). A global model-based description is especially important when using massive proper motion measurements to search for substructure. While radial velocity data are superior at large distances, searches based on proper motions should be better within a few kpc due to high completeness and much larger sample size. A user-friendly interface to our model code, which will allow generation of mock catalogs in an arbitrary direction (or across the entire sky) and to an arbitrary depth, will be described elsewhere (Jurić et al., in preparation).

Monoceros stream is clearly detected as a major outlier from the smooth model presented here. We have not found any other large substructure within 10 kpc that deviates at a detectable level. Other deviations from the smooth model predictions are likely due to systematic errors in the proper motion and radial velocity measurements. However, since the main goal of this paper was to quantify overall kinematic behavior, the emphasis of our analysis was on the first and second moments of the kinematic quantities. It is likely that more sophisticated statistical methods, such as those discussed by Schlaufman et al.

(2009, in preparation) and Klement et al. (2009), will be more efficient in searching for substructure. As an example, we have verified that a moving group discovered by Majewski (1992) is reproduceable with our data.

6.4.   Future Surveys

The results presented here will be greatly extended by numerous upcoming surveys. First, the Gaia mission will provide kinematic measurements to approximately the same faint limit as in our data, but covering the whole sky (Perryman et al. 2001; Wilkinson et al. 2005) and with much smaller systematic errors. Second, several large-scale, deep optical surveys, including the Dark Energy Survey (Flaugher 2008), Pan-STARRS (Kaiser et al. 2002), and the Large Synoptic Survey Telescope (Ivezić et al. 2008), will extend the faint limit of this and the Gaia sample by $4 - 6$ mag. For example, LSST will obtain proper motion measurements of comparable accuracy to those of Gaia at their faint limit, and smoothly extend the error vs. magnitude curve deeper by 5 mag (for details see Eyer et al., in preparation). With its u-band data, LSST will enable studies of metallicity and kinematics using the *same* stars out to a distance of ~ 100 kpc (~ 200 million F/G main sequence stars brighter than $g = 23.5$, for discussion see I08). For comparison, one of the best measurements of the outer halo radial velocity dispersion to date is based on only 241 objects (Battaglia et al. 2005). These upcoming studies are thus certain to provide valuable new information about the formation and evolution of our Galaxy.

A.   The Revised SDSS Metallicity Scale

Recent analysis of the metallicity and kinematics of halo and disk stars by I08 utilized photometric metallicity estimates for F/G stars with $0.2 < g - r < 0.6$. Their mapping function from the $g - r$ vs. $u - g$ color-color diagram to metallicity was calibrated using stars with spectroscopic metallicities distributed in SDSS Data Release 6. At that time, high-metallicity stars required for the calibration of methods implemented in the automated spectroscopic pipeline (SEGUE Stellar Parameters Pipeline, Beers et al. 2006) were not available. Between Data Releases 6 and 7, the required data were collected and the new calibration resulted in the revised spectroscopic metallicity values distributed with Data Release 7 (Lee et al. 2008; Allende Prieto et al. 2008).

Here, we recalibrate the photometric metallicity estimator using updated spectroscopic metallicities from Data Release 7. In addition, we rederive the parts of the I08 analysis that are most affected by this change in the metallicity scale.

A.1.   The updated photometric metallicity estimator

As shown in Figure A1, the largest difference between the SDSS spectroscopic metallicity values distributed with Data Releases 6 and 7 is, as expected, at the high-metallicity end. In particular, the abrupt cutoff in the metallicity distribution at $[Fe/H] \sim -0.5$ (see figure 9 in I08) is no longer present and the distribution extends to values as high as $[Fe/H] \sim -0.2$ (the distances for the stars shown range from ~ 1 kpc to ~ 7 kpc).

We proceed to rederive the photometric metallicity calibration using the same selection criteria and the same methodology as in I08. The new data set admits a slightly simpler

function – the double definition of the x axis is no longer required and the new expression is

$$[Fe/H]_{ph} = A + Bx + Cy + Dxy + Ex^2 + Fy^2 + Gx^2y + Hxy^2 + Ix^3 + Jy^3, \qquad \text{(A1)}$$

with $x = (u - g)$ and $y = (g - r)$. The best-fit coefficients are $(A - J) = (-13.13, 14.09, 28.04, -5.51, -5.90, -58.68, 9.14, -20.61, 0.0, 58.20)$. Note that the coefficient, I, is zero. We removed this term because it was producing too much curvature at the right end (red $u - g$) of the best-fit map.

We estimate that an upper limit on the intrinsic metallicity scatter for fixed noiseless $u - g$ and $g - r$ colors (presumably due to limited sensitivity of broadband colors to metallicity variations) is about 0.1 dex. This value is estimated from the scatter in the difference between spectroscopic and photometric metallicities, discussed below. Unlike I08, who simply adopted the median metallicity value given by the above expression for each star, we draw photometric metallicity estimates from a Gaussian distribution centered on the best-fit median value, and with a width of 0.1 dex. The main benefit to this is that we avoid hard edges in the photometric metallicity distribution for stars close to the edges of the calibration region in the $g - r$ vs. $u - g$ diagram.

The performance of the new map is qualitatively similar to that of the old map. The difference between spectroscopic and photometric metallicities as a function of the $g - r$ and $u - g$ colors are shown in the top two panels of Figure A2. Typical systematic errors in the map (i.e. median difference per pixel) are ~ 0.1 dex or smaller, and the scatter varies from ~ 0.2 dex at the high-metallicity end to ~ 0.3 dex at the low-metallicity end (note that this scatter includes a contribution from errors in both spectroscopic and photometric metallicities).

The above photometric metallicity estimator is applicable for stars with $0.2 < g - r < 0.6$ and $-0.25 + 0.5 * (u - g) < g - r < 0.05 + 0.5(u - g)$; that is, for main-sequence F and G stars in the calibration region of the $g - r$ vs. $u - g$ color-color diagram (top two panels

of Figure A2). For stars with spectroscopic metallicity $[Fe/H] > -2.2$, the distribution of the difference between spectroscopic and photometric metallicities is well described by a Gaussian with a width of 0.26 dex (see the bottom right panel in Figure A2).

It should be noted that the performance of the photometric metallicity estimator deteriorates at the low-metallicity end because the $u - g$ color becomes insensitive to decreases in metallicity. As shown in the bottom left panel of Figure A2, the photometric metallicity saturates at $[Fe/H] \sim -2$ for smaller values of spectroscopic metallicity. Even at $[Fe/H] = -2$, the true metallicity is overestimated by $0.2 - 0.3$ dex, and by $[Fe/H] = -3$ this bias is as large as 1 dex (photometric metallicity values never become significantly lower than $[Fe/H] = -2$). This shortcoming could be partially alleviated by employing more accurate u-band photometry (say, with errors of 0.01 mag instead of 0.03 mag, as used here), but probably not for metallicities lower than $[Fe/H] = -2.5$. Fortunately, the low-metallicity halo stars within SDSS reach have a median metallicity of $[Fe/H] \sim -1.5$ (I08), so for the majority of stars the photometric metallicitoies are robust. Another important note is that, despite the improvement at the high-metallicity end, the calibration range only extends to $[Fe/H] \sim -0.2$. Our calibration sample did not include young, metal-rich main-sequence stars ($u - g > 1.1$ and $g - r < 0.3$). For this reason, our polynomial model underestimates true metallicities by $0.2 - 0.3$ dex at $[Fe/H] = 0$, and probably more for $[Fe/H] > 0$. Any result relying on higher metallicities should be interpreted with caution (especially at low galactic latitudes where the uncertain ISM extinction may strongly affect the estimated metallicities). We plan to extend our calibration further into the metal-rich domain by employing data from the SDSS-II SEGUE survey.

A.2. Tomography II reloaded

I08 pointed out several aspects of their analysis that may have been affected by the metallicity "compression" at the high-metallicity end in DR6. We repeated their full analysis and report here on those aspects where differences warrant discussion.

The "hard" upper limit on photometric metallicity estimates at the high-metallicity end ($[Fe/H] \sim -0.5$) with the DR6 calibration is best seen in the bottom left panel in figure 9 from I08. We reproduce that map of the conditional metallicity distribution in the top left panel of Figure A3. As expected, the metallicity distribution of disk stars within 2 kpc of the Galactic plane now extends to $[Fe/H] \sim 0$.

In the new calibration, the parameters describing the variation of the median metallicity for disk stars as a function of the distance from the Galactic plane,

$$\mu_D(Z) = \mu_\infty + \Delta_\mu \, \exp(-|Z|/H_\mu) \text{ dex}, \tag{A2}$$

are also changed. The updated values are $H_\mu = 0.5$ kpc, $\mu_\infty = -0.82$ and $\Delta_\mu = 0.55$ (the old values were $H_\mu = 1.0$ kpc, $\mu_\infty = -0.78$ and $\Delta_\mu = 0.35$). The best-fit values of μ_∞ and Δ_μ are accurate to ~ 0.05 dex. Values of H_μ in the range $350 - 700$ pc are consistent with the data – the decrease in H_μ is required by the local constraint, $\mu_D(Z) = -0.2$ (Nordström et al. 2004; Allende Prieto et al. 2004).

An interesting result from I08 was detection of disk stars at a distance from the Galactic plane as large as ~ 6 kpc (see their figure 10). A peak at $[Fe/H] = -0.5$ in the metallicity distribution of stars at those distances was another manifestation of the metallicity "compression". As demonstrated in the top right panel of Figure A3, this peak is not present when using the revised calibration. However, there is still statistical evidence that disk stars exist at these large distances from the plane: about 5% of stars in the $5 < Z < 7$ kpc bin are consistent with disk stars, in agreement with extrapolation of the

exponential profile derived from stellar counts.

Perhaps the most intriguing result of I08 was the non-detection of a correlation between rotational velocity and metallicity for disk stars at $Z \sim 1$ kpc. At such distances from the Galactic plane, the counts of thin and thick disk stars are expected to be similar. Since traditionally the thick disk component is associated with a larger velocity lag and lower metallicities, a fairly strong and detectable correlation was expected (see I08 for details). The two bottom panels in Figure A3 demonstrate that such a correlation is still undetected, although the photometric metallicity range now extends to higher values (up to $[Fe/H] \sim -0.2$).

The higher metallicity values obtained with the re-calibrated relation have a quantitative effect on the best-fit metallicity distributions shown in figure 7 of I08. Using the same methodology, we reproduce the metallicity distributions with the new calibration in Figure A4. I08 modeled the non-Gaussian disk metallicity distribution using a sum of two Gaussians with a fixed amplitude ratio (1.7:1), fixed difference of the mean values (0.14 dex), and fixed widths (0.21 dex and 0.11 dex), which "slides" as a function of Z according to Equation A2. We find that the only significant change is an increase to the width of the second Gaussian to 0.21 dex, which accounts for the extension of the metallicity distribution to higher values. Only minor changes are required for the best-fit halo metallicity distribution (see table 3 in I08): the median halo metallicity is now -1.46 in the first three bins, and -1.56 in the most distant Z bin, and its width changed from 0.32 dex to 0.36 dex in the last bin. We note somewhat less scatter of the data points around the best-fit functions with the re-calibrated data set. To summarize, the revised best-fit parameters that describe halo and disk metallicity distributions are:

- The halo metallicity distribution is spatially invariant and well described by a Gaussian distribution centered on $[Fe/H] = -1.46$, and with an intrinsic (not

including measurement errors) width $\sigma_H = 0.30$ dex. For $|Z| \lesssim 10$ kpc, an upper limit on the halo radial metallicity gradient is 0.005dex kpc^{-1}.

- The disk metallicity distribution varies with Z such that its shape remains fixed, while its median, μ_D, varies as given by Equation A2 (with the best-fit parameter values $H_\mu = 0.5$ kpc, $\mu_\infty = -0.82$, and $\Delta_\mu = 0.55$). The shape of the disk metallicity distribution can be modeled as

$$p_D(x = [Fe/H]|Z) = 0.63\,G[x|\mu = a(Z), \sigma = 0.2] + 0.37\,G[x|\mu = a(Z) + 0.14, \sigma = 0.2],$$
$$\text{(A3)}$$

where the position a and the median μ_D are related via $a(Z) = \mu_D(Z) - 0.067$ (unless measurement errors are very large).

We point out that the asymmetry of the metallicity distribution for disk stars is now less pronounced (as implied by the same widths of the two best-fit Gaussian components). Nevertheless, due to our large sample size, the non-gaussianity is detected at high significance. A remaining uncertainty is the error distribution of the photometric metallicities, which itself could account for such a deviation from gaussianity. However, to the extent possible using a highly incomplete spectroscopic sample (c.f. the bottom right panel in Figure A2 and discussion in I08), we are unable to quantitatively explain the observed deviation from gaussianity as an artifact of the photometric metallicity method.

B.   SQL Query Example

The following SQL query was used to select and download data for all SDSS stars with spectroscopic and proper motion measurements (see http://casjobs.sdss.org/CasJobs).

```
SELECT
```

```
    round(p.ra,6) as ra, round(p.dec,6) as dec,

    p.run, p.rerun, round(p.extinction_r,3) as rExt,

    round(p.psfMag_u,2) as upsf,  --- comments are preceeded by ---

    round(p.psfMag_g,2) as gpsf,  --- rounding up

    round(p.psfMag_r,2) as rpsf,

    round(p.psfMag_i,2) as ipsf,

    round(p.psfMag_z,2) as zpsf,

    round(p.psfMagErr_u,2) as uErr,

    round(p.psfMagErr_g,2) as gErr,

    round(p.psfMagErr_r,2) as rErr,

    round(p.psfMagErr_i,2) as iErr,

    round(p.psfMagErr_z,2) as zErr,

    round(s.pmL,2) as pmL, round(s.pmB,2) as pmB, pmRaErr,

    t.specObjID, t.plate, t.mjd, t.fiberid, t.feha, t.fehaerr,

    t.logga, t.loggaerr, t.elodierv, t.elodierverr
INTO mydb.pmSpec
FROM star p, propermotions s, sppParams t, specobjall q
WHERE
    p.objID = s.objID and s.match = 1 --- must have proper motion

    and t.specobjid = q.specobjid and q.bestobjid = p.objid

    and s.sigra < 350 and s.sigdec < 350  --- quality cut on pm

    and (p.flags & '4295229440') = 0  --- see text for flag list

    and p.psfMag_r > 14.5  --- avoid saturation

    and p.psfMag_r < 20    --- practical faint limit for pm
--- the end of query
```

The following `SQL` query was used to select and download data for all spectroscopically confirmed quasars with proper motion measurements and redshifts in the range $0.5 - 2.5$.

```
SELECT
  round(p.ra,6) as ra, round(p.dec,6) as dec,
  p.run, p.rerun, round(p.extinction_r,3) as rExt,
  round(p.psfMag_u,2) as upsf,
  round(p.psfMag_g,2) as gpsf,
  round(p.psfMag_r,2) as rpsf,
  round(p.psfMag_i,2) as ipsf,
  round(p.psfMagErr_u,2) as uErr,
  round(p.psfMagErr_g,2) as gErr,
  round(p.psfMagErr_r,2) as rErr,
  round(p.psfMagErr_i,2) as iErr,
  round(s.pmL,2) as pmL, round(s.pmB,2) as pmB, pmRaErr,
  q.specObjID, q.plate, q.mjd, q.fiberID,
  q.z, q.zErr, q.zConf, q.zWarning, q.specClass
INTO mydb.pmQSO
FROM star p, propermotions s, specobjall q
WHERE
  p.objID = s.objID and s.match = 1
  and q.bestobjid = p.objid
  and s.sigra < 350 and s.sigdec < 350 -- per \citet{Munn04}
  and (p.flags & '4295229440') = 0
  and p.psfMag_r > 14.5
  and p.psfMag_r < 20
  and q.z > 0.5    --- redshift limits
```

```
   and q.z < 2.5

--- the end of query
```

REFERENCES

Allende Prieto, C., Barklem, P. S., Lambert, D. L., & Cunha, K. 2004, A&A, 420, 183

Allende Prieto, C., Beers, T. C., Wilhelm, R., Newberg, H. J., Rockosi, C. M., Yanny, B., & Lee, Y. S. 2006, ApJ, 636, 804

Allende Prieto, C. et al. 2008, AJ, 136, 2070

Battaglia, G. et al. 2005, MNRAS, 364, 433

Beers, T. C., Lee, Y., Sivarani, T., Allende Prieto, C., Wilhelm, R., Fiorentin, P. R., Bailer-Jones, C., Norris, J. E., & the SEGUE Calibration Team. 2006, Memorie della Societa Astronomica Italiana, 77, 1171

Binney, J. & Tremaine, S. 2008, Galactic Dynamics, Princeton Series in Astrophysics, Princeton University Press, Princeton and Oxford

Binney, J. & Merrifield, M. 1998, Galactic Astronomy, Princeton Series in Astrophysics, Princeton University Press, Princeton

Bochanski, J. J., Munn, J. A., Hawley, S. L., West, A. A., Covey, K. R., & Schneider, D. P. 2007, AJ, 134, 2418

Bramich, D. M. et al. 2008, MNRAS, 386, 887

Carollo, D. et al. 2007, Nature, 450, 1020

Dehnen, W. 1998, AJ, 115, 2384

Dehnen, W. & Binney, J. J. 1998, MNRAS, 298, 387

De Simone, R.S., Wu, X. & Tremaine, S. 2004, MNRAS, 350, 627

Eggen, O. J., Lynden-Bell, D., & Sandage, A. R. 1962, ApJ, 136, 748

Eggen, O. J. 1996, AJ, 112, 1595

Eisenhauer, F. et al. 2003, ApJ, 597, L121

Feast, M. W. & Whitelock, P. 1997, MNRAS, 291, 683

Flaugher, B. 2008, in A Decade of Dark Energy: Spring Symposium, Proceedings of the conferences held May 5-8, 2008 in Baltimore, Maryland. (USA). Edited by Norbert Pirzkal and Henry Ferguson. http://www.stsci.edu/institute/conference/spring2008

Fuchs, B. et al. 2009, AJ, 137, 4149

Gilmore, G., Wyse, R. F. G., & Kuijken, K. 1989, ARA&A, 27, 555

Grillmair, C. J. & Dionatos, O. 2006, ApJ, 643, L17

Gunn, J. E., Knapp, G. R., & Tremaine, S. D. 1979, AJ, 84, 1181

Rocha-Pinto, H.J., Flynn, C., Scalo, J. 2004, å, 423, 517

Helmi, A. 2008, A&A Rev., 15, 145

Ivezić, Ž. et al. 2004, Astronomische Nachrichten, 325, 583

Ivezić, Ž. et al. 2005, in Astronomical Society of the Pacific Conference Series, Vol. 338, Astrometry in the Age of the Next Generation of Large Telescopes, ed. P. K. Seidelmann & A. K. B. Monet, 201–+

—. 2006, Memorie della Societa Astronomica Italiana, 77, 1057

—. 2008, ApJ, 684, 287

Jurić, M. et al. 2008, ApJ, 673, 864

Kaczmarczik, M. C., Richards, G. T., & Schlegel, D. 2007, in Bulletin of the American Astronomical Society, Vol. 38, Bulletin of the American Astronomical Society, 798–+

Kaiser, N. et al. 2002, in Society of Photo-Optical Instrumentation Engineers (SPIE) Conference Series, Vol. 4836, Society of Photo-Optical Instrumentation Engineers (SPIE) Conference Series, ed. J. A. Tyson & S. Wolff, 154–164

Klement, R. et al. 2009, ApJ, 698, 865

Lee, Y. S. et al. 2008, AJ, 136, 2022

Loebman, S. et al. 2008, in American Institute of Physics Conference Series, Vol. 1082, American Institute of Physics Conference Series, 238–242

Majewski, S. R. 1992, ApJS, 78, 87

—. 1993, ARA&A, 31, 575

Munn, J. A. et al. 2004, AJ, 127, 3034

Murray, C.A. 1986, MNRAS, 223, 649

Nordström, B. et al. 2004, A&A, 418, 989

Perryman, M. A. C. et al. 2001, A&A, 369, 339

Robin, A. C., Reylé, C., Derrière, S., & Picaud, S. 2003, A&A, 409, 523

Roškar, R., Debattista, V. P., Quinn, T. R., Stinson, G. S., & Wadsley, J. 2008, ApJ, 684, L79

Schneider, D. P. et al. 2007, AJ, 134, 102

Sesar, B., Ivezić, Ž., & Jurić, M. 2008, ApJ, 689, 1244

– 59 –

Siebert, A. et al. 2008, MNRAS, 391, 793

Smith, M. C. et al. 2009, ArXiv e-prints

Wilkinson, M. I. et al. 2005, MNRAS, 359, 1306

York, D. G. et al. 2000, AJ, 120, 1579

Table 1.   Best-fit parameters[a] for the disk velocity distribution[b].

Quantity	a	b	c
$\bar{v}_\phi{}^1$	-194	19.2	1.25
σ_ϕ^1	12	1.8	2.0
σ_ϕ^2	34	1.2	2.0
σ_ϕ^D	30	3.0	2.0
σ_R	40	5.0	1.5
σ_Z	25	4.0	1.5

The uncertainties are typically ~ 10km s^{-1} for a, $\sim 20\%$ for b and 0.1-0.2 for c.

[a]All listed quantities are modeled as $a + b|Z|^c$, with Z in kpc, and velocities in km s^{-1}.

[b]The v_ϕ distribution is non-gaussian, and can be formally described by a sum of two gaussians with a fixed normalization ratio f_k:1, with $f_k = 3$. The mean value for the second gaussian has a fixed offset from the first gaussian, $\bar{v}_\phi{}^2 = (\bar{v}_\phi{}^1 - \Delta\bar{v}_\phi)$, with $\Delta\bar{v}_\phi = 34$ km/s. Extrapolation beyond $Z > 5$ kpc is not reliable. The velocity dispersion for the second gaussian is given by σ_ϕ^2. If this non-gaussianity is ignored, the v_ϕ dispersion is given by σ_ϕ^D.
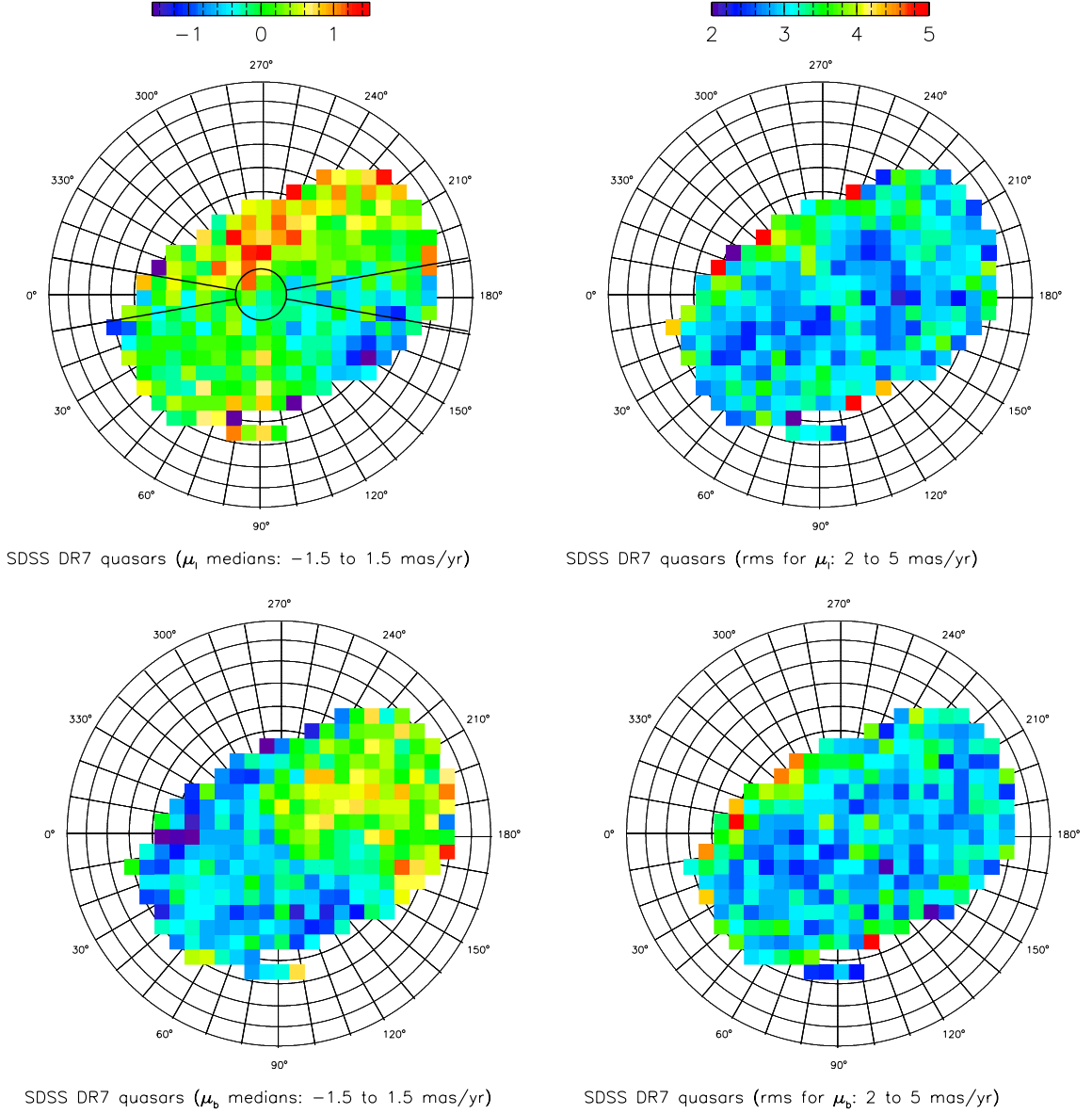
Fig. 1.— Behavior of proper motion measurements for $60,000$ spectroscopically confirmed SDSS quasars with galactic latitude $b > 0$. The color-coded maps (see the legend on top, units are mas yr^{-1}) show the distribution of the median (left) and rms (right) for the longitudinal (top) and latitudinal (bottom) proper motion components in a Lambert projection of the northern Galactic cap. The median number of quasars per pixel is ~ 250. For both components, the scatter across the sky is 0.60 mas yr^{-1}. The median proper motion for the full quasar sample is 0.15 mas yr^{-1} in the longitudinal direction, and -0.20 mas yr^{-1} in the latitudinal direction. The thick line in the top left panel shows the selection boundary for
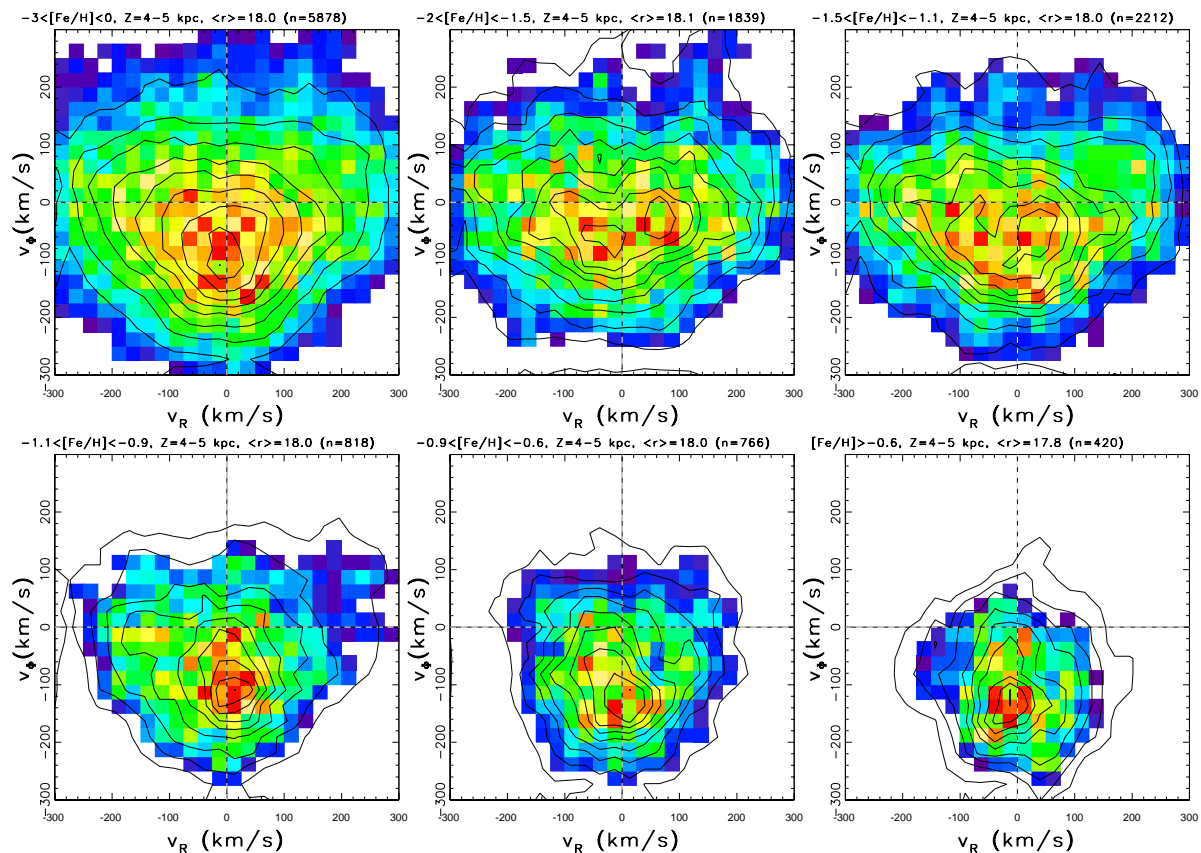
Fig. 2.— Change of the v_Φ vs. v_R velocity distribution with metallicity, at an approximately constant R and Z. Velocities are determined from proper motion measurements. The top left panel shows the v_Φ vs. v_R diagram for $\sim 6,000$ blue ($0.2 < g-r < 0.4$) stars at $Z = 4-5$ kpc and detected towards the North Galactic Pole ($b > 80°$). The distribution is shown using linearly-spaced contours, and with color-coded map showing smoothed counts in pixels (low-to-high from blue-to-red). The other five panels are analogous and show subsamples selected by metallicity, with the $[Fe/H]$ range listed above each panel (also listed are the median r-band magnitude and subsample size). The measurement errors are typically 70 km s^{-1}. Note the strong variation of median v_Φ with metallicity.
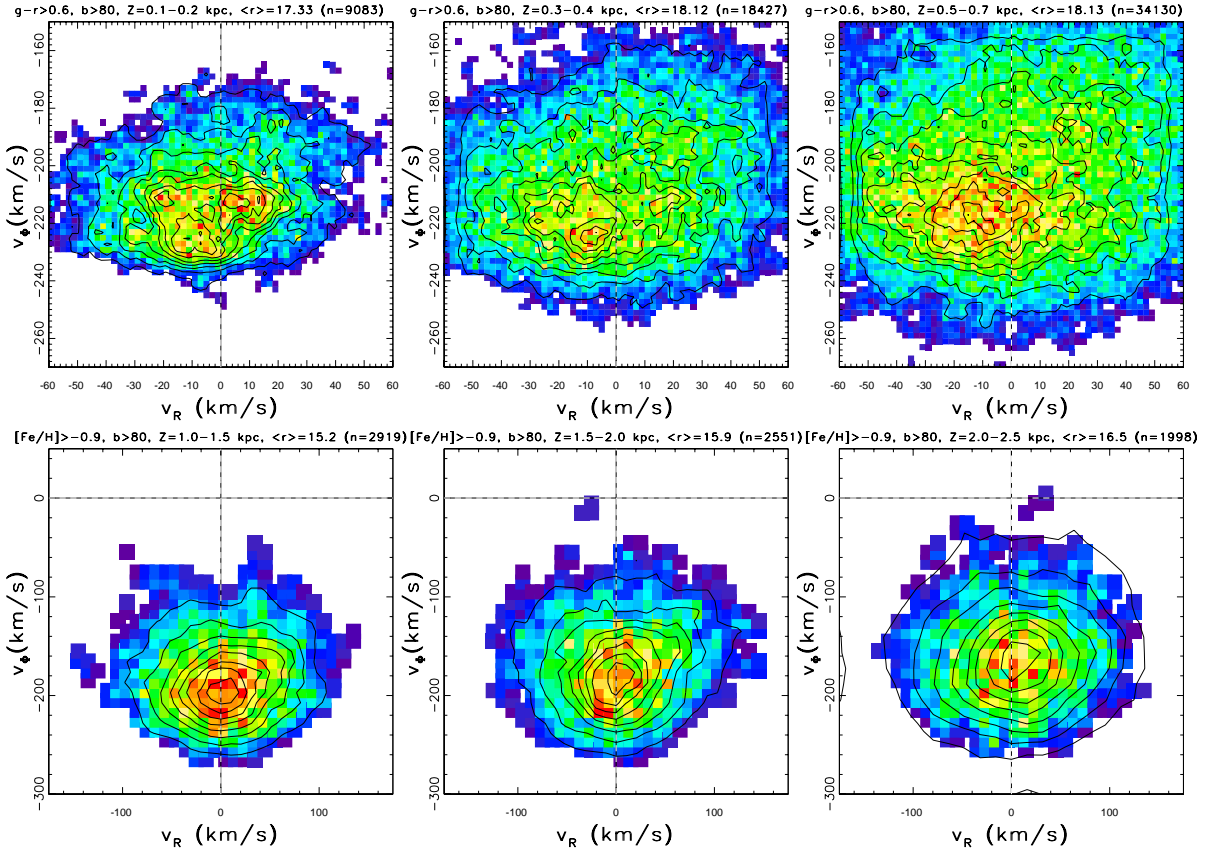
Fig. 3.— Similar to Figure 2, except that the v_Φ vs. v_R velocity distribution is plotted for a range of Z. The top row shows the v_Φ vs. v_R diagrams for $\sim 60{,}000$ red ($g-r > 0.6$) stars at $Z = 100 - 700$ pc and observed towards the North Galactic Pole. Each panel corresponds to a narrow range in Z, given above each panel. The measurement errors vary from ~ 3 km s^{-1} in the closest bin to ~ 12 km s^{-1} in the most distant bin. Note the complex multi-modal substructure in the top left panel. The bottom three panels are analogous and show the v_Φ vs. v_R diagrams for $\sim 7{,}000$ blue ($0.2 < g-r < 0.4$) stars with high metallicity ($[Fe/H] > -0.9$). The measurement errors vary from ~ 20 km s^{-1} in the closest bin to ~ 35 km s^{-1} in the most distant bin. Note that the median v_Φ approaches zero as Z increases.
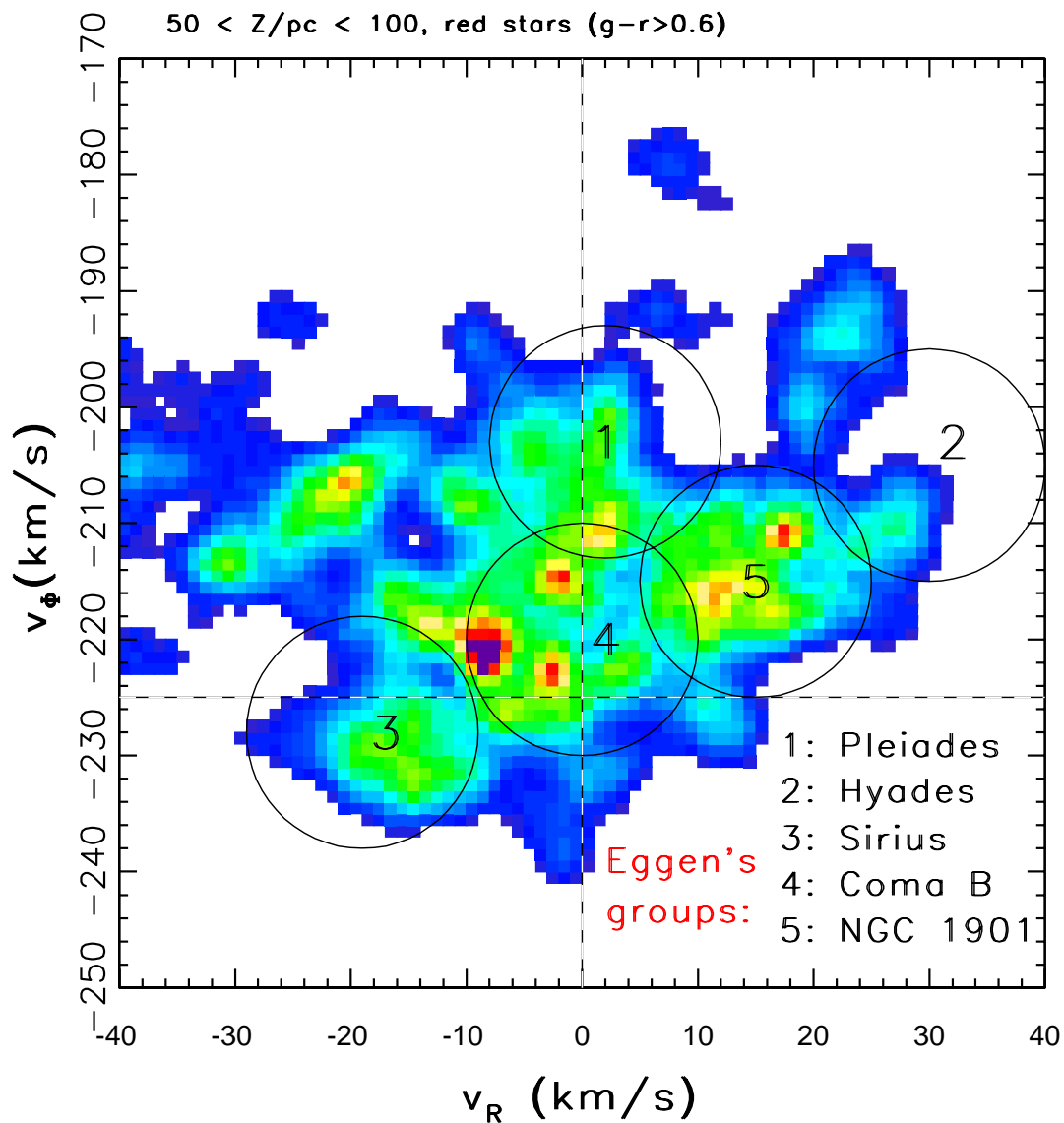
Fig. 4.— Similar to the top left panel in Figure 3, except that stars are selected from a distance bin that corresponds to HIPPARCOS sample ($Z = 50 - 100$ pc). The positions of Eggen's moving groups (Eggen 1996) are marked by circles, according to the legend in the bottom right corner.
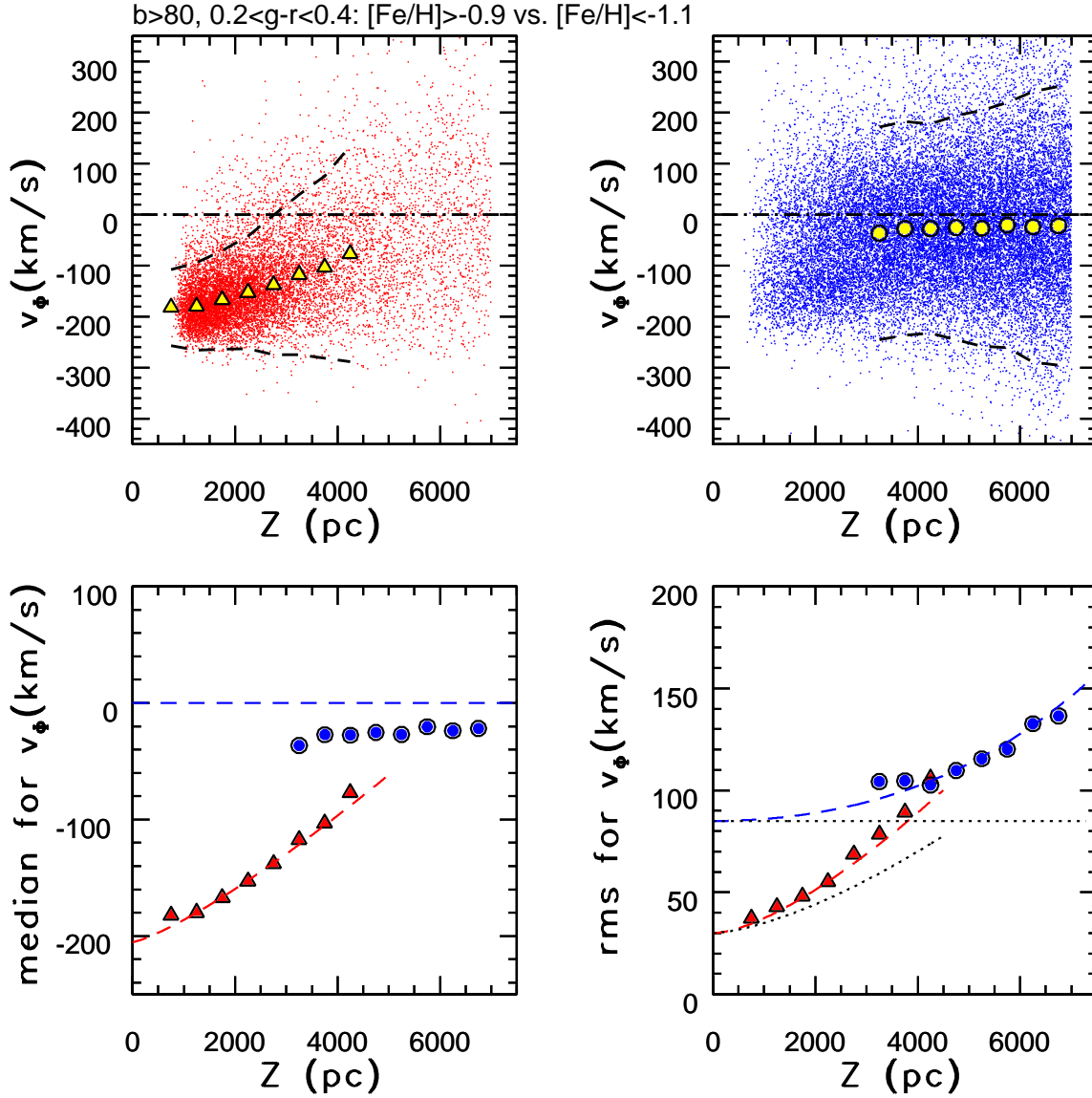
Fig. 5.— Dependence of the rotational velocity, v_Φ, on distance from the plane for $14,000$ high-metallicity ($[Fe/H] > -0.9$; top left panel) and $23,000$ low-metallicity ($[Fe/H] < -1.1$, top right) stars with $b > 80°$. In the top two panels, individual stars are plotted as small dots, and the medians in bins of Z are plotted as large symbols. The 2σ envelope around the medians is shown by dashed lines. The bottom two panels compare the medians (left) and dispersions (right) for the two subsamples shown in the top panels and the dashed lines in the bottom two panels show predictions of a kinematic model described in text. The dotted lines in the bottom right panel show model dispersions without a correction for measurement errors.
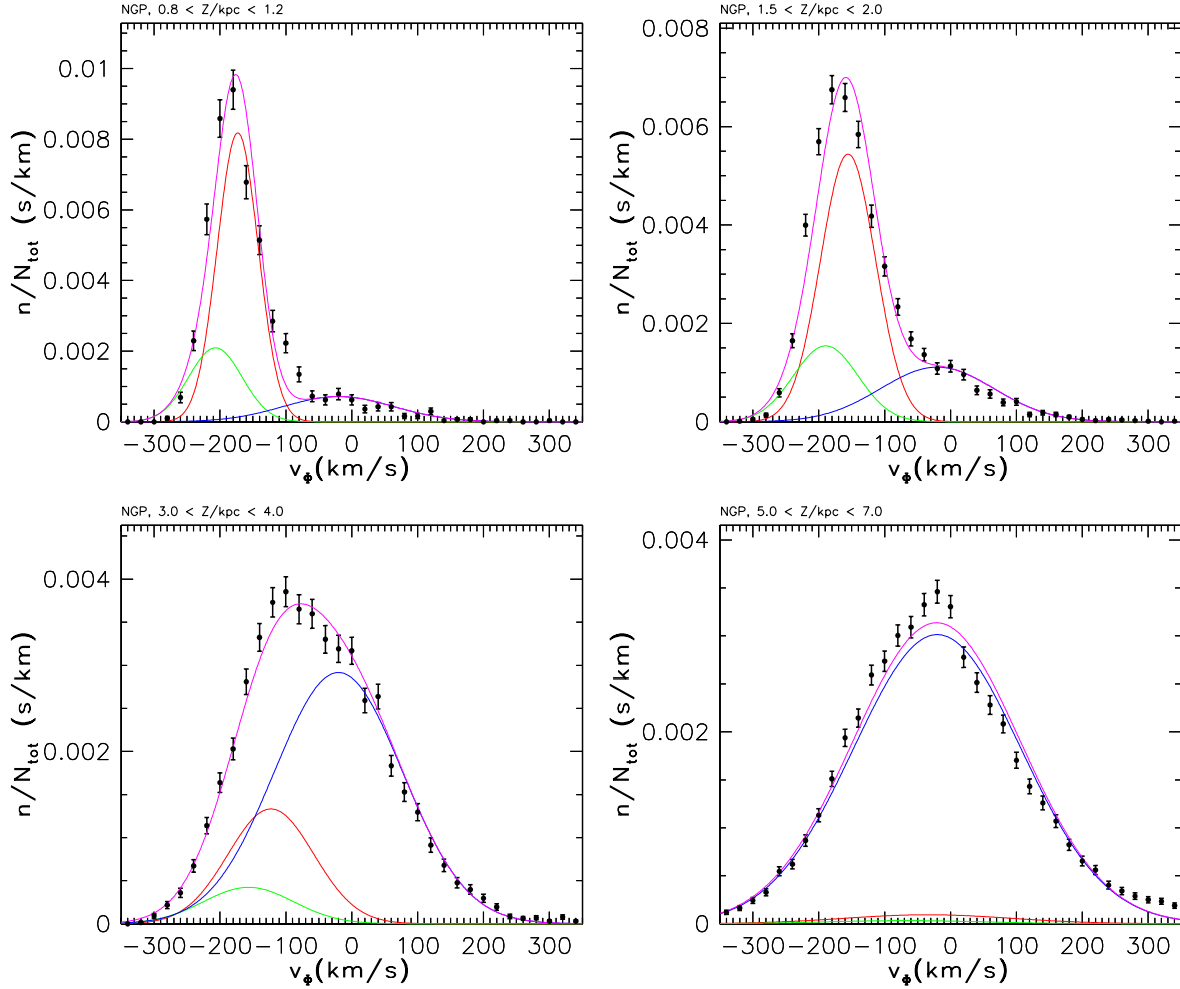
Fig. 6.— Symbols with error bars are the measured rotational velocity distribution, v_Φ, for stars with $0.2 < g - r < 0.4$, $b > 80°$, and $Z = 0.8 - 1.2$ kpc (top left, $\sim 1,500$ stars), $1.5 - 2.0$ kpc (top right, $\sim 4,100$ stars), $3.0 - 4.0$ kpc (bottom left, $\sim 6,400$ stars) and $5.0 - 7.0$ kpc (bottom right, $\sim 12,500$ stars). The red and green curves show the contribution of a two-component disk model (see Equations 18 and 19), the blue curves show the gaussian halo contribution, and the magenta curves are their sum.
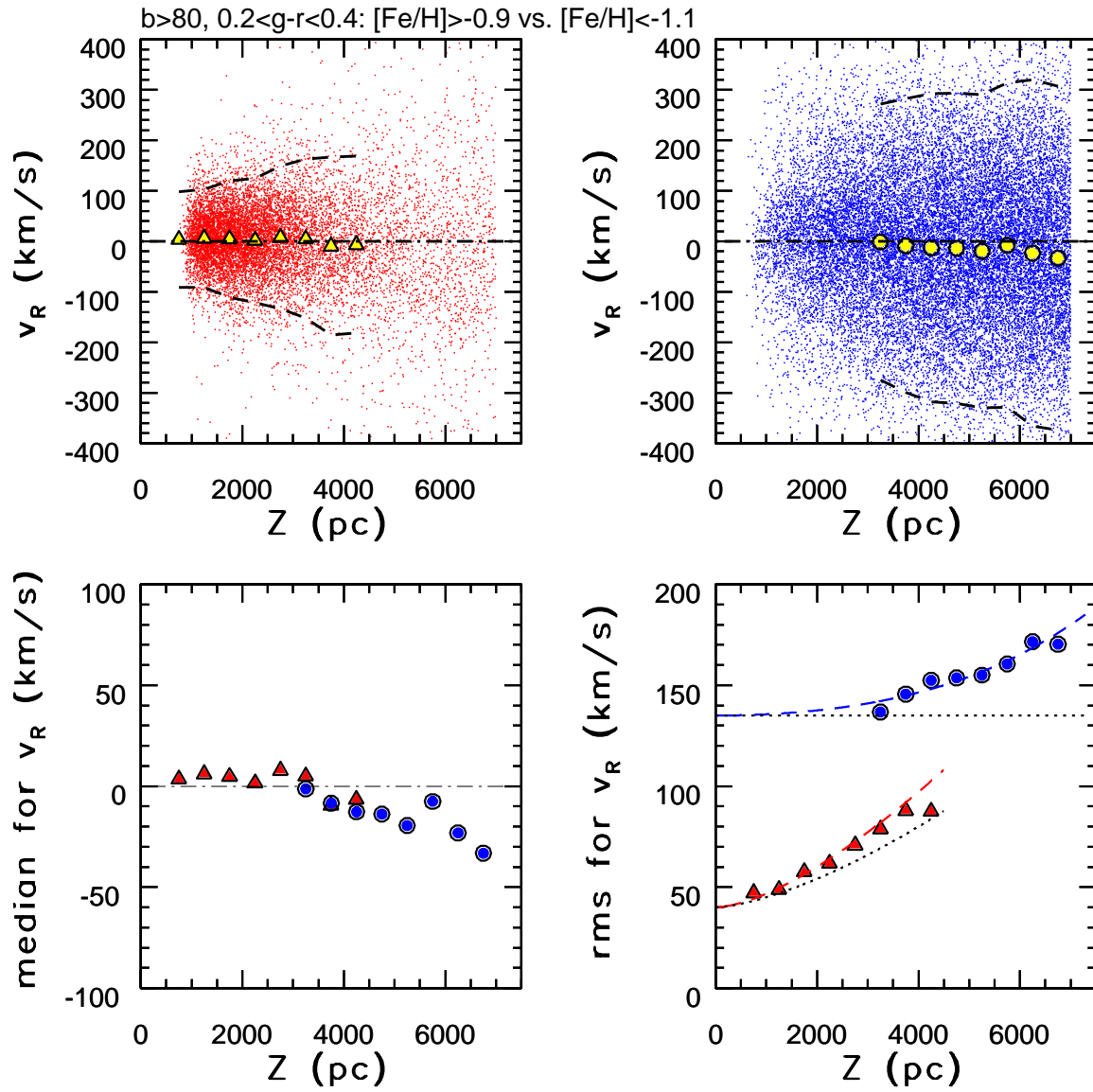
Fig. 7.— Analogous to Figure 5, but for the radial velocity component, v_R.
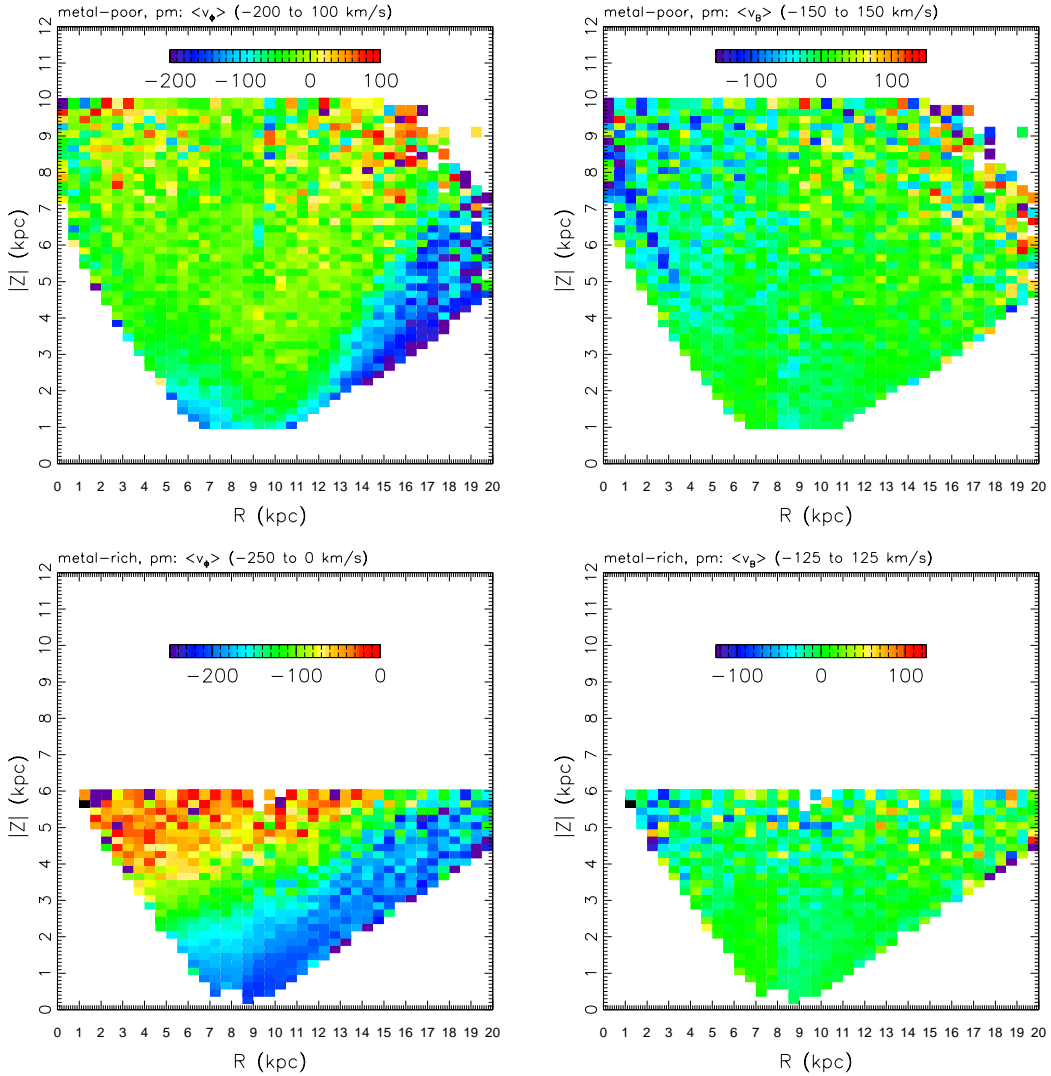
Fig. 8.— Dependence of velocity, measured using proper motions, on cylindrical galactocentric coordinates for 172,000 metal-poor halo stars ($[Fe/H] < -1.1$; top panels) and 205,000 metal-rich disk-like stars ($[Fe/H] > -0.9$; bottom panels). Stars are selected from three regions, including $b > 80°$ (the North Galactic pole), $170° < l < 190°$ (anticenter), and $350° < l < 10°$ (center) and the left column plots rotational velocity, v_Φ, while the right column plots $v_B = \sin(b)v_R + \cos(b)v_Z$. To aid visualization of these boundaries, see the thick line in the top left panel in Figure 1. The median values of velocity in each bin are color-coded according to the legend shown in each panel. The measurements are reliable at distances up to about 7 kpc, but regions beyond this limit are shown for halo stars for completeness. The fraction of disk stars is negligible at such distances, and their velocity distribution is shown for $Z < 6$ kpc. The region with negative velocity on the right side of top left panel is due to contamination of the halo sample by stars from Monoceros stream. The thin region with negative velocity on the left side of top right panel is a data artifact
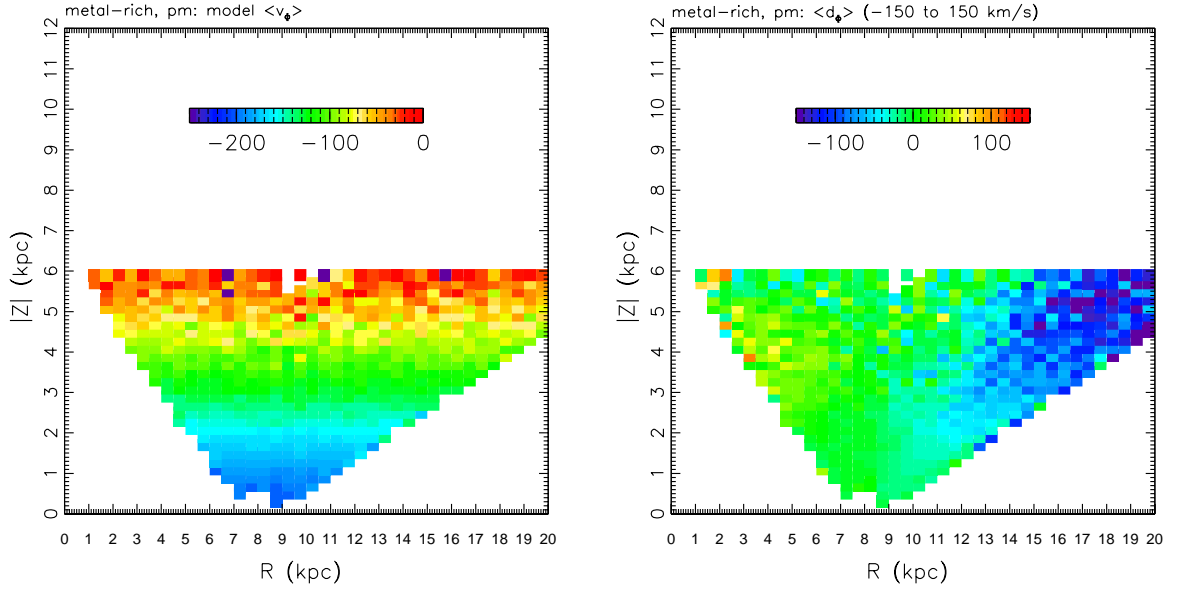
Fig. 9.— Left panel is analogous to the bottom left panel in Figure 8, but for a model described in the text. The right panel shows the median difference between the data and model. Large discrepancies at $R > 12$ kpc are due to Monoceros stream (at $R = 18$ kpc and $Z = 4$ kpc, disk stars rotate with a median $v_\phi \sim -100$ km s^{-1}, while for Monoceros stream, $v_\phi \sim -200$ km s^{-1}).
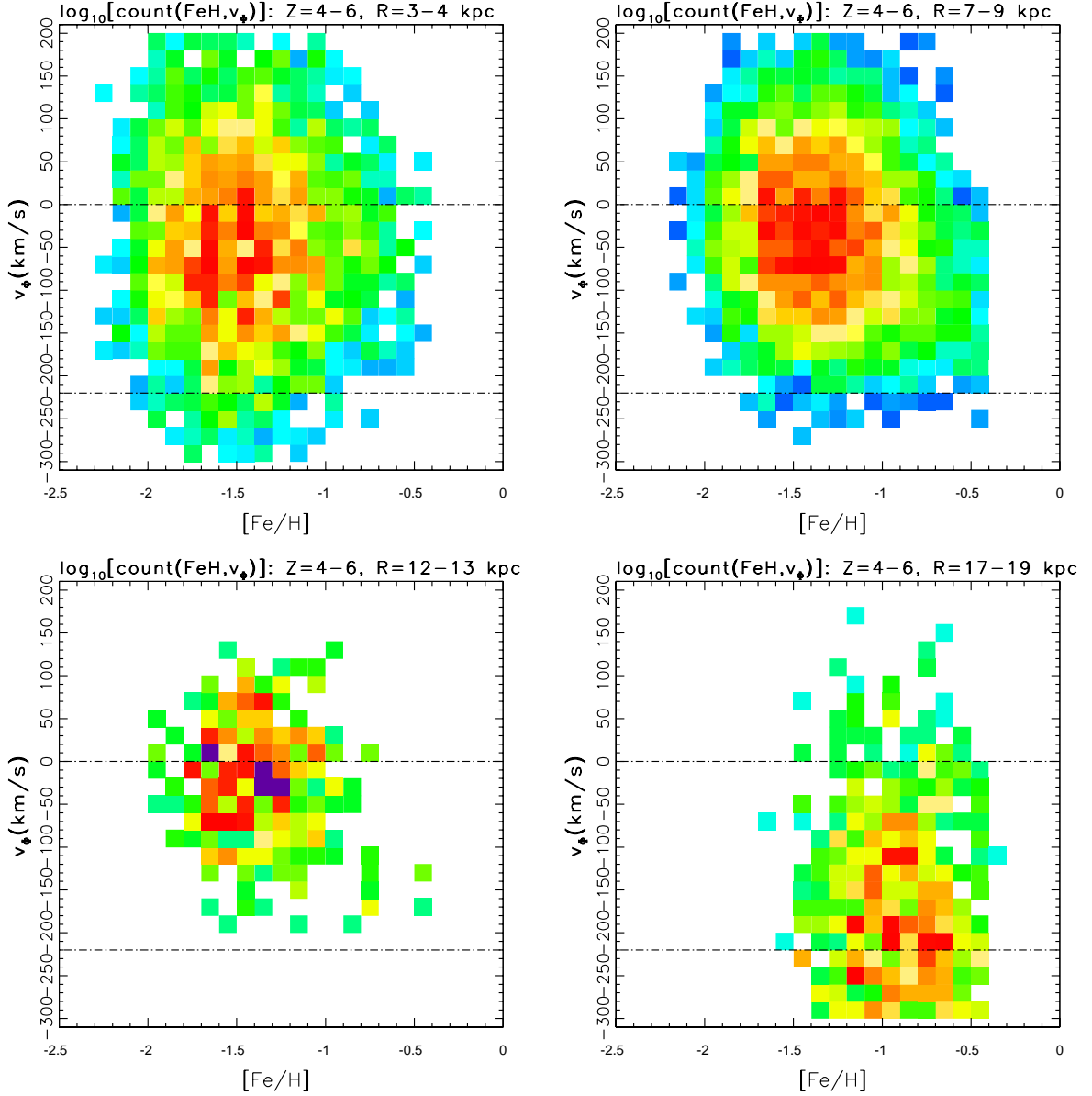
Fig. 10.— Distribution of stars with $0.2 < g - r < 0.4$ and $Z = 4 - 6$ kpc in the rotational velocity vs. metallicity plane, for four ranges of galactocentric cylindrical radius, R (top left: $3 - 4$ kpc; top right: $7 - 9$ kpc; bottom left: $12 - 13$ kpc; bottom right: $17 - 19$ kpc). In each panel, the color-coded map shows the logarithm of counts in each pixel, scaled by the total number of stars. The horizontal lines at $v_\Phi = 0$ km s^{-1} and $v_\Phi = -220$ km s^{-1} are added to guide the eye. High-metallicity ($[Fe/H] \sim -1$) stars with fast rotation ($v_\Phi \sim -220$ km s^{-1}) visible in the bottom right panel belong to Monoceros stream, and are responsible for features seen at $R > 15$ kpc in the two left panels in Figure 8.
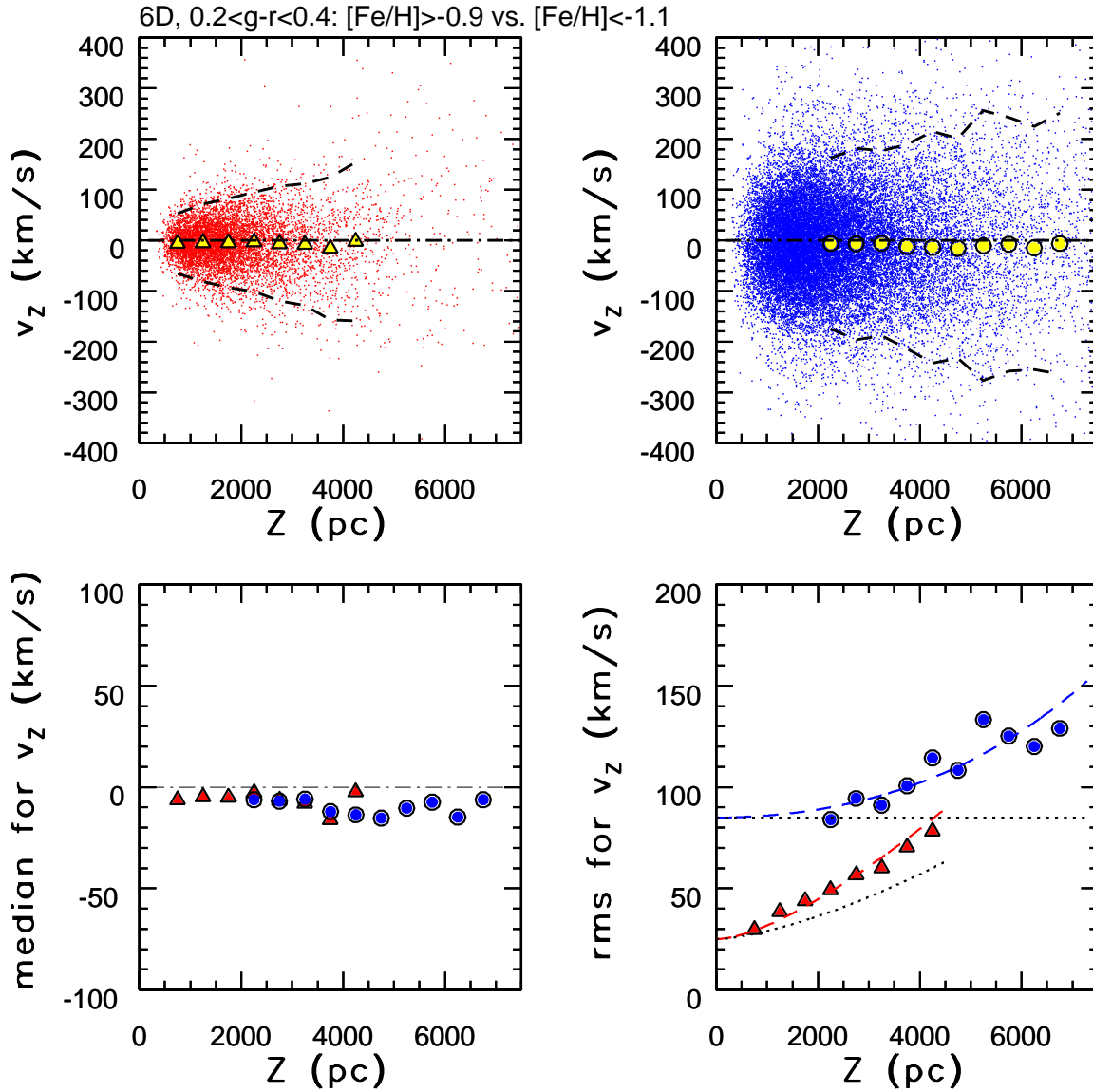
Fig. 11.— Similar to Figure 5, but for the vertical velocity component, v_Z, and using a sample of stars with SDSS radial velocity measurements, $0.2 < g - r < 0.4$ and $b > 20$ (12,000 stars in the high-metallicity subsample, and 38,000 stars in the low-metallicity subsample). An analogous figure for extended samples of 53,000 disk stars and 47,000 halo stars with $0.2 < g - r < 0.6$ look similar. The behavior of the rotational and radial velocity components in this sample is consistent with that shown in Figures 5 and 7.
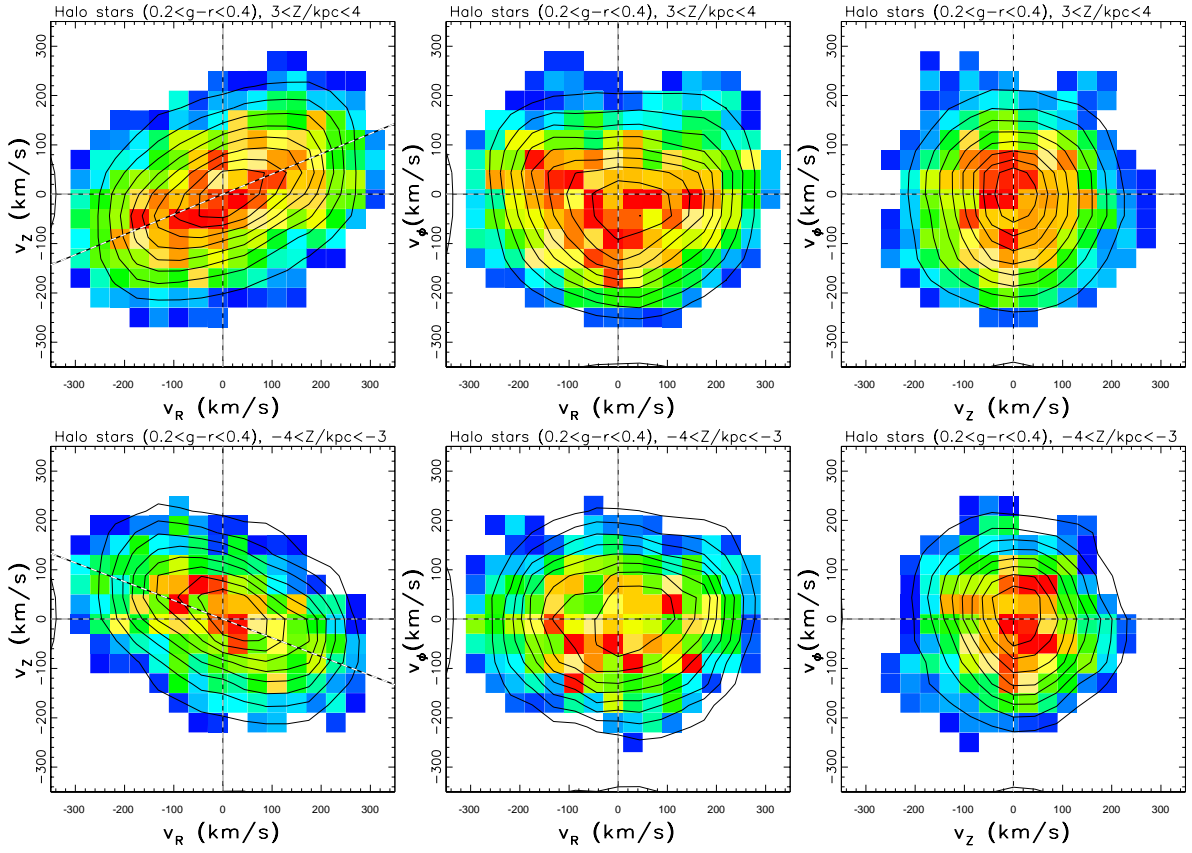
Fig. 12.— Three two-dimensional projections of the velocity distribution for two subsamples of candidate halo stars selected using spectroscopic metallicity $(-3 < [Fe/H] < -1.1)$ and with $6 < R/\text{kpc} < 11$. The top row corresponds to $2,700$ stars with distances from the Galactic Plane, $3 < Z/\text{kpc} < 4$, and the bottom row to $1,300$ stars with $-4 < Z/\text{kpc} < -3$. The distributions are shown using linearly-spaced contours, and with a color-coded map showing smoothed counts in pixels (low-to-high from blue-to-red). The measurement errors are typically 60 km s^{-1}. Note the strong evidence for velocity ellipsoid tilt in top and bottom left panels (see also Fig. 13). The two dashed lines in these panels show the median direction towards the Galactic center.
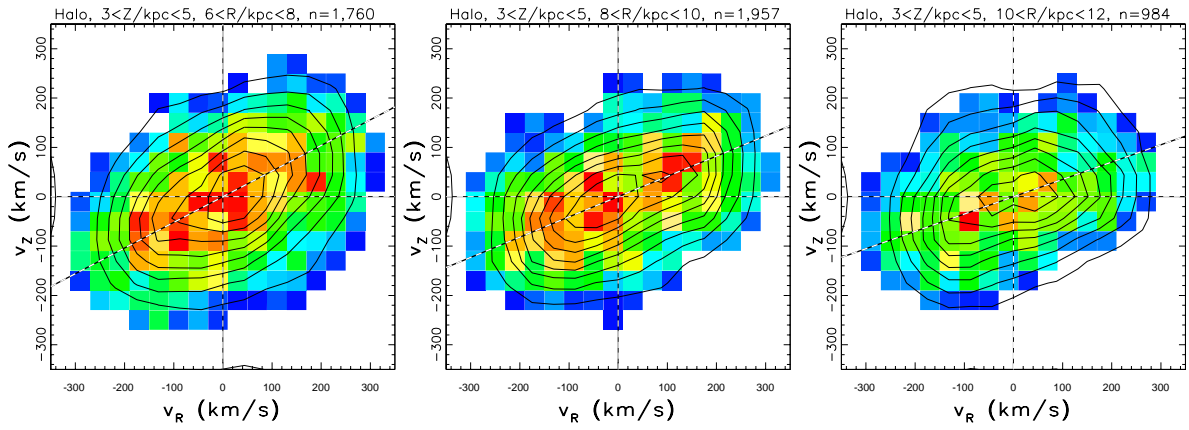
Fig. 13.— An illustration of the velocity ellipsoid tilt angle variation. Analogous to Fig. 12, except that only the v_Z vs. v_R projection is shown for a constant Z, and three ranges of R, as marked on the top of each panel.
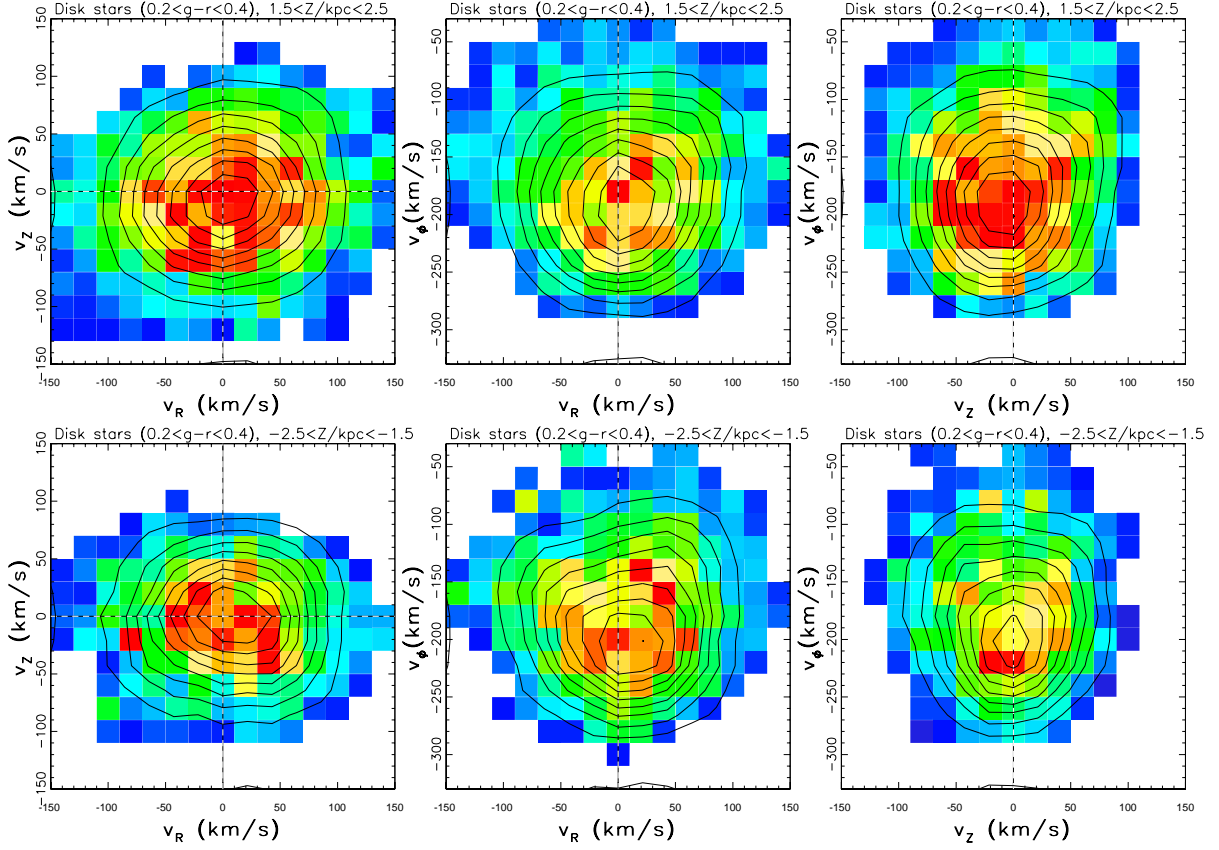
Fig. 14.— Analogous to Figure 12, except that the velocity distribution is shown for two subsamples of candidate disk stars selected using spectroscopic metallicity ($[Fe/H] > -0.9$). The top row corresponds to $2,200$ stars with distances from the galactic plane $1.5 < Z/\text{kpc} < 2.5$, and the bottom row to $1,500$ stars with $-2.5 < Z/\text{kpc} < -1.5$. The measurement errors are typically 35 km s^{-1}. Note the absence of velocity ellipsoid tilt in top and bottom left panels.
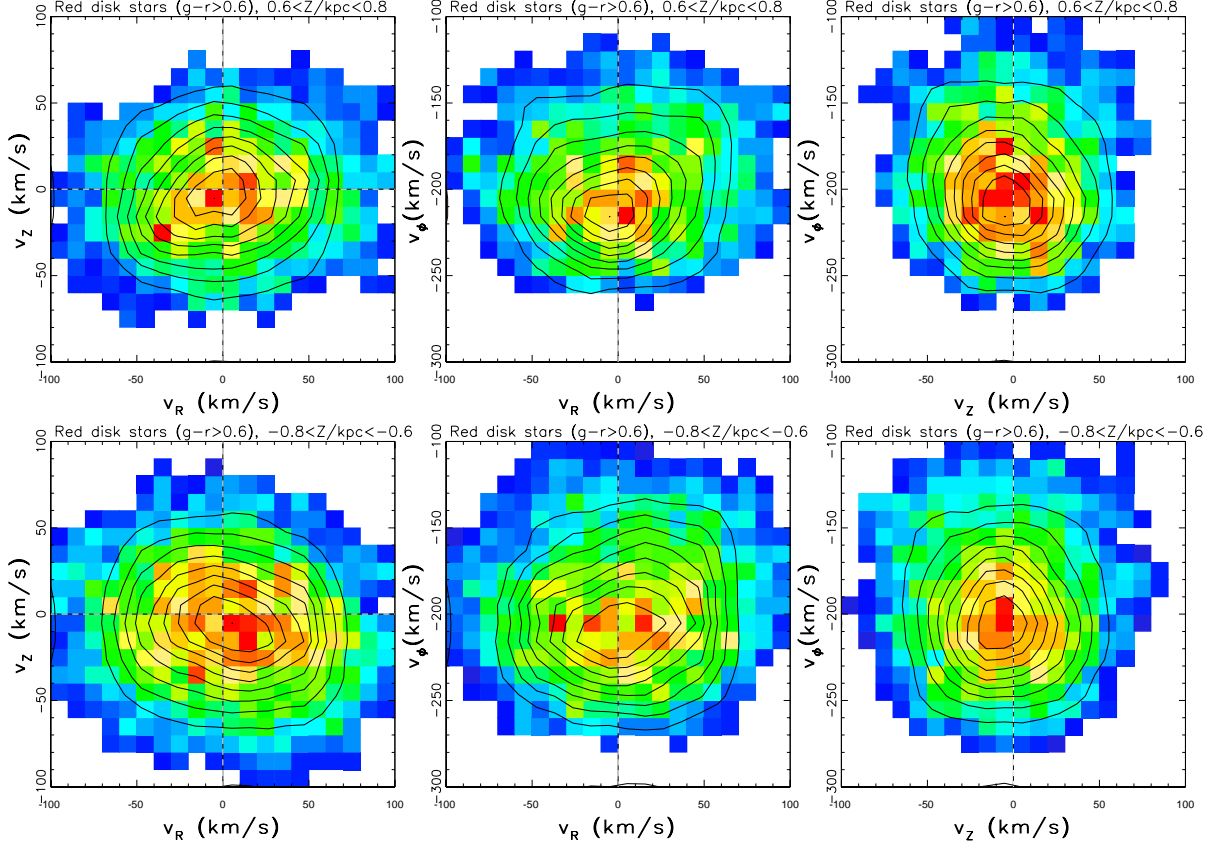
Fig. 15.— Analogous to Figure 14, except that the velocity distribution is shown for two subsamples of red stars $(g-r > 0.6)$: the top row corresponds to $3,000$ stars with distances from the galactic plane $0.6 < Z/\mathrm{kpc} < 0.8$, and the bottom row to $4,600$ stars with $-0.8 < Z/\mathrm{kpc} < -0.6$. The measurement errors are typically ~ 15 km s^{-1}.
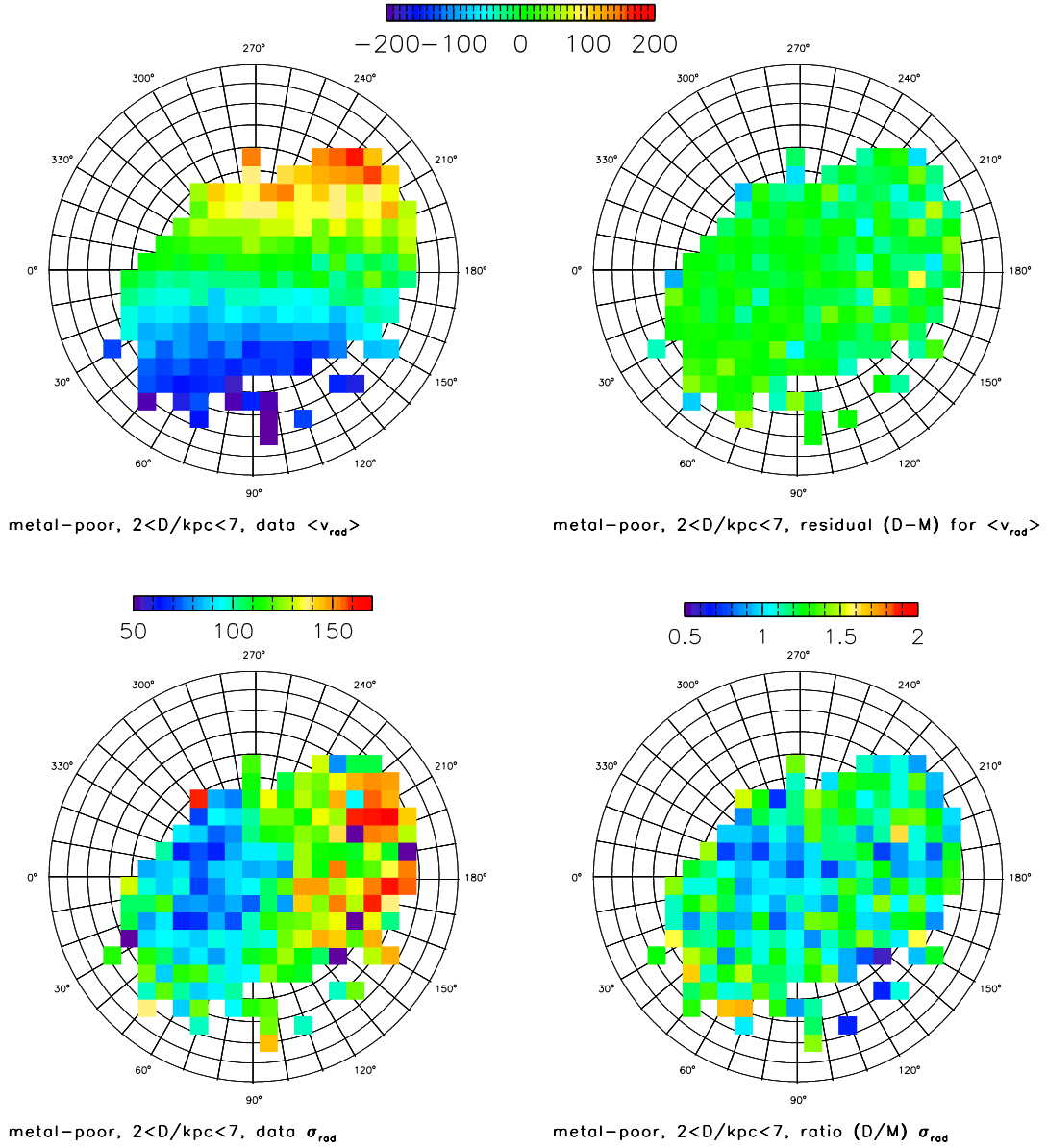
Fig. 16.— Comparison of medians and dispersions for the measured and modeled radial velocity of $20,000$ blue ($0.2 < g - r < 0.4$) halo stars (spectroscopic $[Fe/H] < -1.1$) at distances, $D = 2 - 7$ kpc, and $b > 20°$. The top left panel shows the median measured radial velocity in each pixel, color-coded according to the legend shown at the top (units are km s^{-1}). The top right panel shows the difference between this map and an analogous map based on model-generated values of radial velocity, using the same scale as in the top left panel. The bottom left panel shows the dispersion of measured radial velocities, color-coded according to the legend above it. The bottom right panel shows the ratio of this map and an analogous map based on model-generated values of radial velocity, color-coded according to the legend above it. When the sample is divided into 1 kpc distance shells, the behavior is similar.
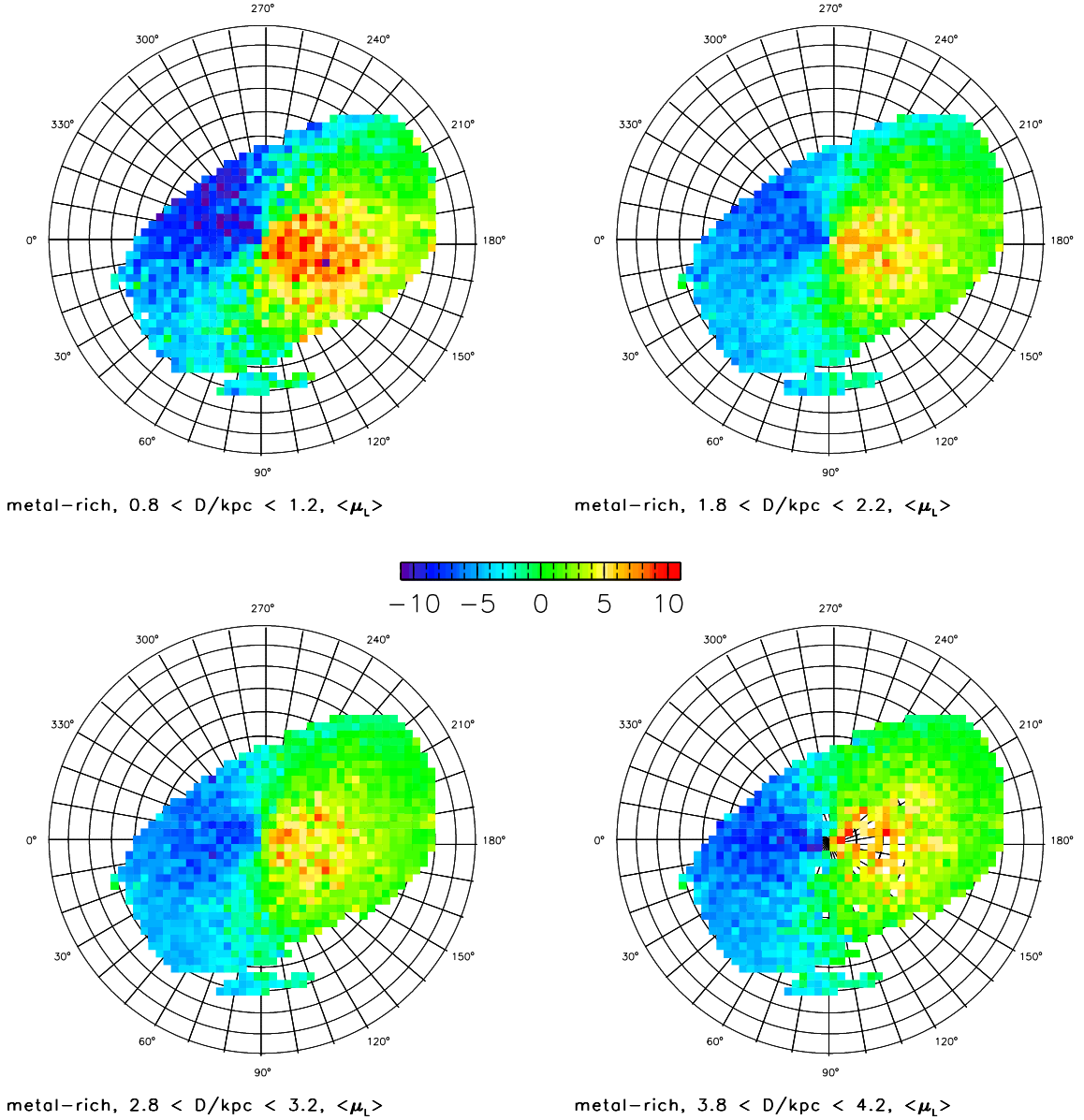
Fig. 17.— Distribution of the median longitudinal proper motion in a Lambert projection of the northern Galactic cap for high-metallicity ($[Fe/H] > -0.9$), blue ($0.2 < g - r < 0.4$) stars, in several distance bins (top left: $58,000$ stars with $D = 0.8 - 1.2$ kpc; top right: $119,000$ stars with $D = 1.8 - 2.2$ kpc; bottom left: $72,000$ stars with $D = 2.8 - 3.2$ kpc; bottom right: $43,000$ stars with $D = 3.8 - 4.2$ kpc). All maps are color-coded using the same scale, shown in the middle (units are mas yr^{-1}). Note that the magnitude of the proper motion does not change appreciably as the distance varies from ~ 2 kpc to ~ 4 kpc. This is due to a vertical gradient in the rotational velocity for disk stars (see Figure 3).
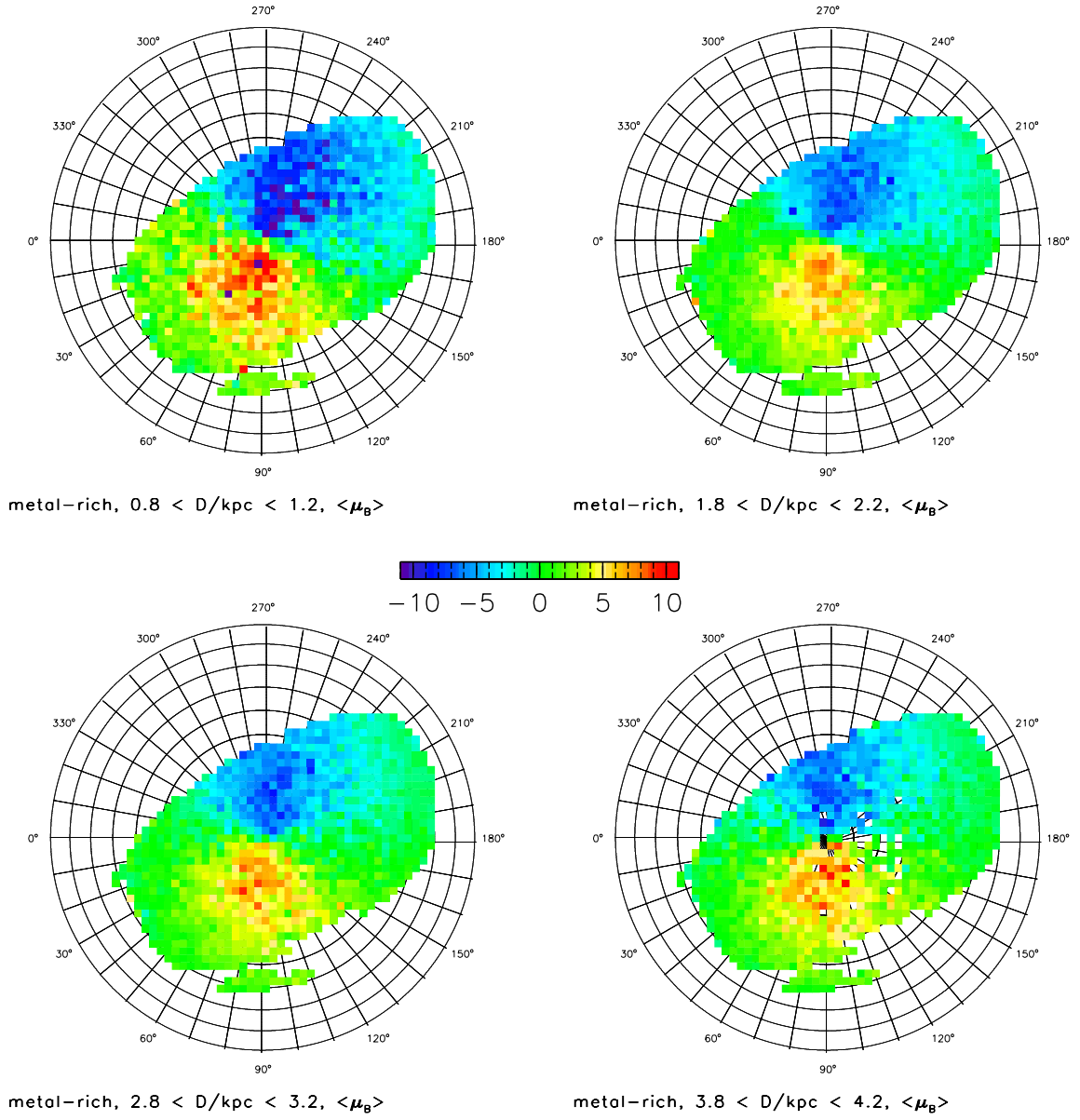
Fig. 18.— Analogous to Figure 17, except that the latitudinal proper motion is shown.

metal−rich, 0.8 < D/kpc < 1.2, μ_L: <residuals>

metal−rich, 1.8 < D/kpc < 2.2, μ_L: <residuals>

metal−rich, 2.8 < D/kpc < 3.2, μ_L: <residuals>

metal−rich, 3.8 < D/kpc < 4.2, μ_L: <residuals>
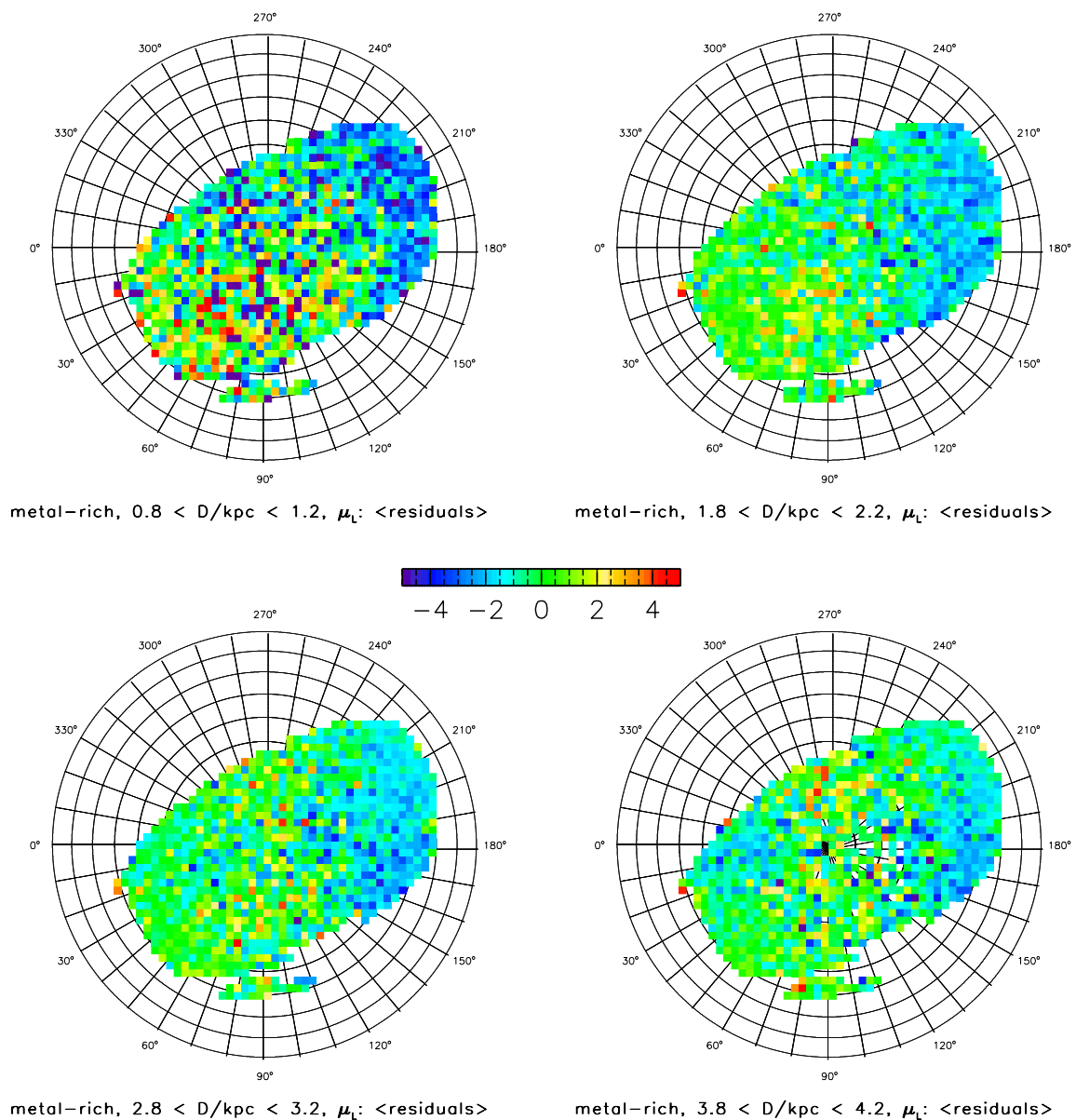
Fig. 19.— Similar to Figure 17, except that the median difference between the observed value of longitudinal proper motion and a value predicted by model described in text is shown. All maps are color-coded using the same scale, shown in the middle. Note that the displayed scale is streched by a factor of two compared to the scale from Figure 17, in order to emphasize discrepancies.
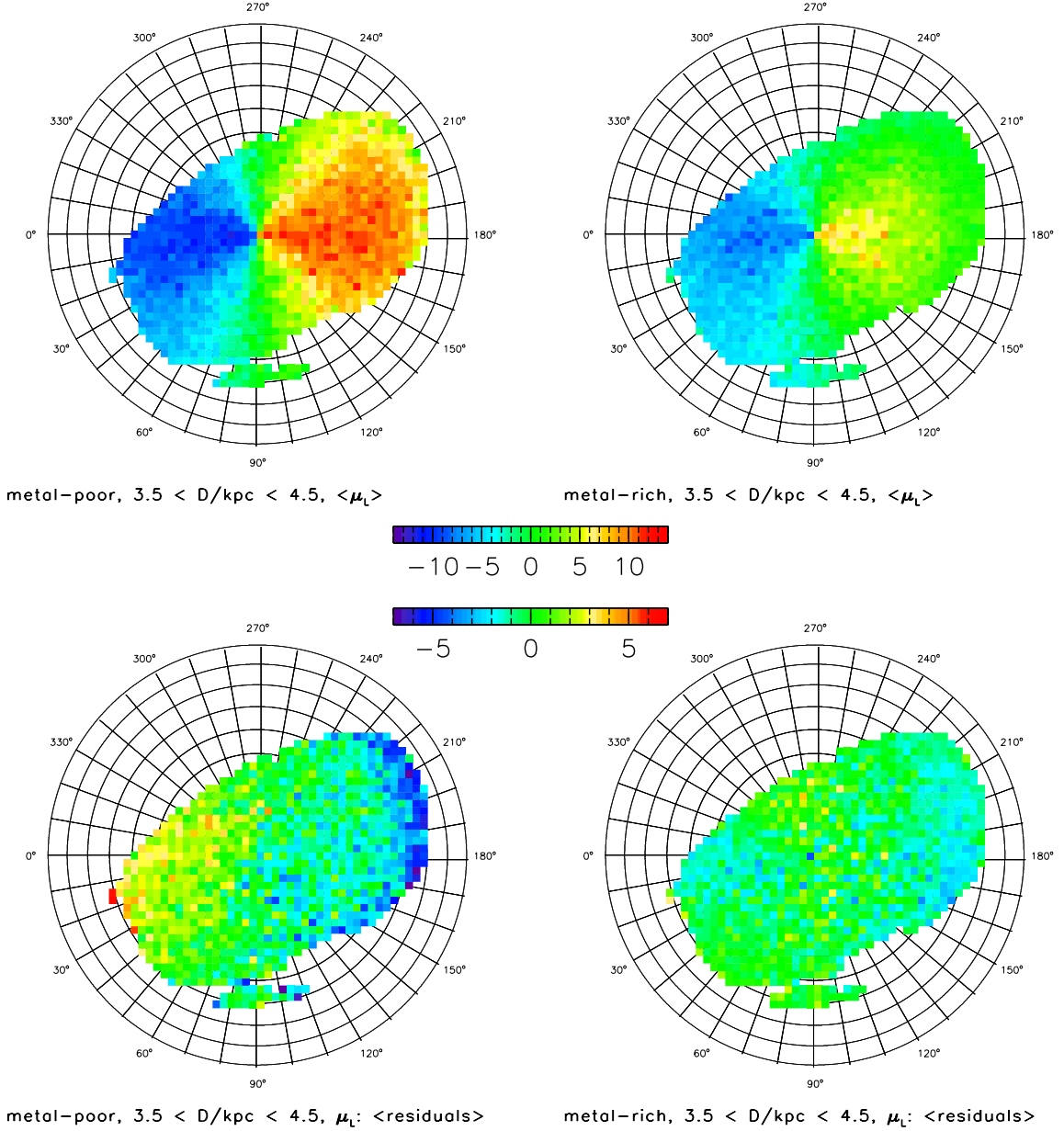
Fig. 20.— Similar to Figures 17 and 19, except that the behavior of high-metallicity (left) and low-metallicity (right) stars is compared in a single distance bin (3.5 − 4.5 kpc). The top two panels show the median longitudinal proper motion, and the two bottom panels show the median difference between the observed and model-predicted values. An analogous figure for the latitudinal proper motion has similar characteristics.
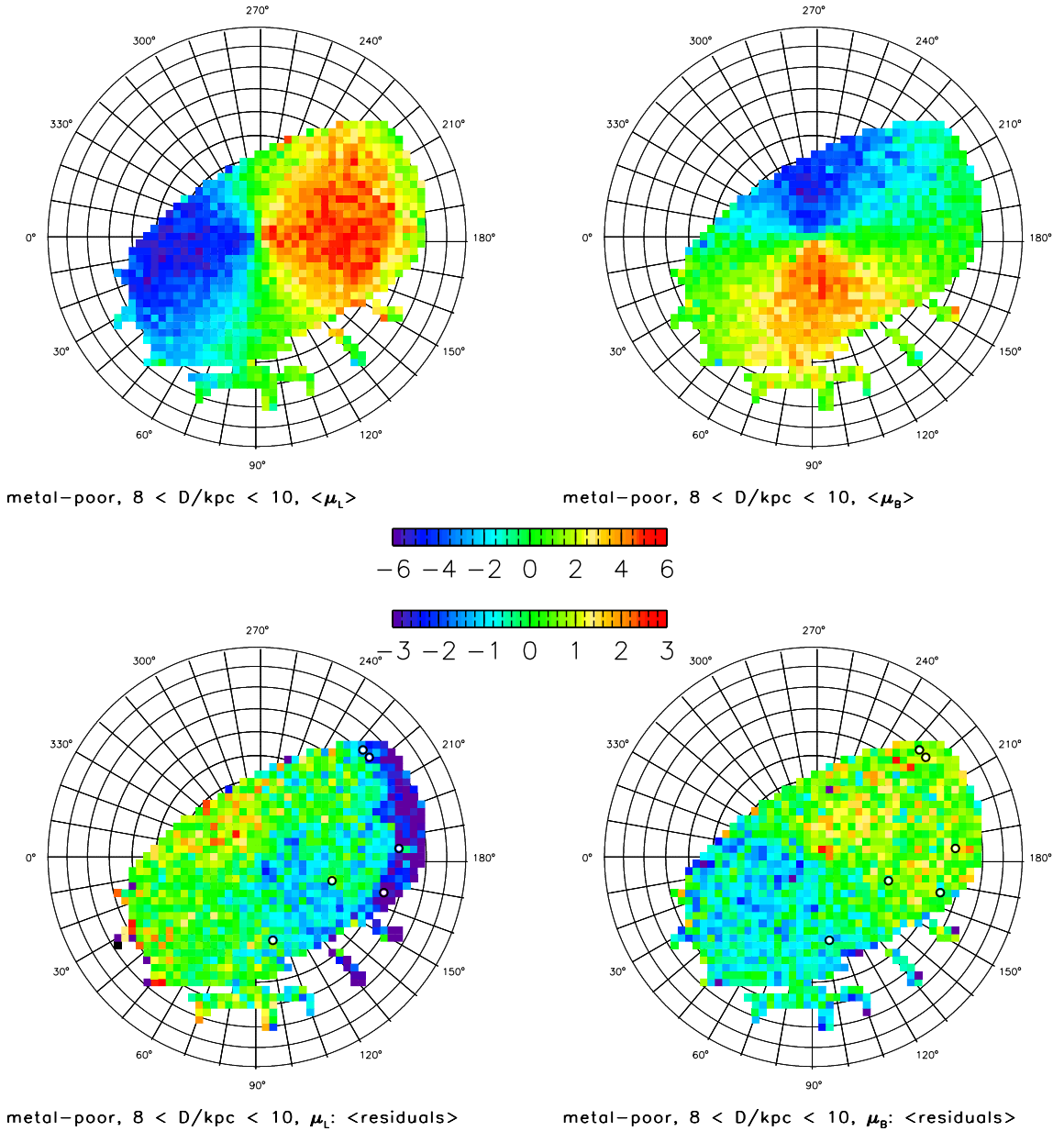
Fig. 21.— Similar to Figure 20, except that the behavior of low-metallicity stars from the $8 - 10$ kpc distance bin is analyzed. The top two panels show the median longitudinal (left) and latitudinal (right) proper motions, and the two bottom panels show the median difference between the observed and model-predicted values. The maps are color-coded according to the legends in the middle (mas yr^{-1}; note that the bottom scale has a harder stretch to emphasize structure in the residual maps). The two bottom panels display very similar morphology to systematic proper motion errors shown in the two left panels in Figure 1. In the bottom panels, the white symbols show the positions of the six northern cold substructers identified by Schlaufman et al. (2009, in preparation).
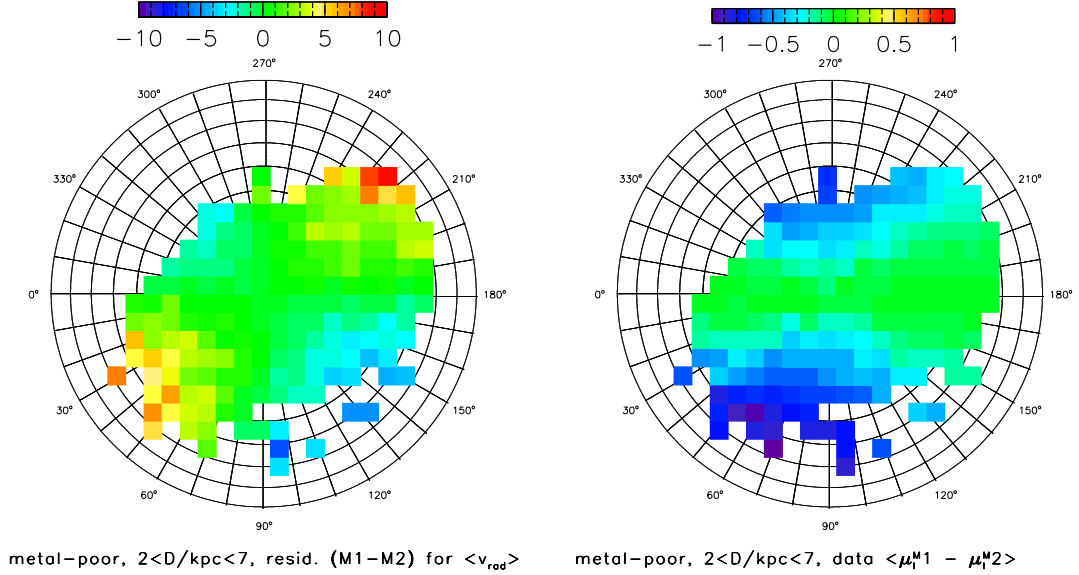
Fig. 22.— Comparison of radial velocity residuals (left panel; analogous to the top right panel in Fig. 16) and longitudinal proper motion residuals (right panel; analogous to the bottom left panel in Fig. 20, except for the larger distance range) for two halo models with $(v_\phi^{halo}, v_{LSR})=$ $(-20,180)$ km s^{-1}, and $(20,220)$ km s^{-1}. Note that we set $v_{LSR} - v_\phi^{halo} = 200$ km s^{-1}. The residuals are color-coded according to the legend above each panel (units are km s^{-1} for the left panel and mas yr^{-1} for the right panel). In order to distinguish these models, systematic errors in radial velocity must be below 10 km s^{-1}, and systematic errors in proper motion must be below 1 mas yr^{-1}.
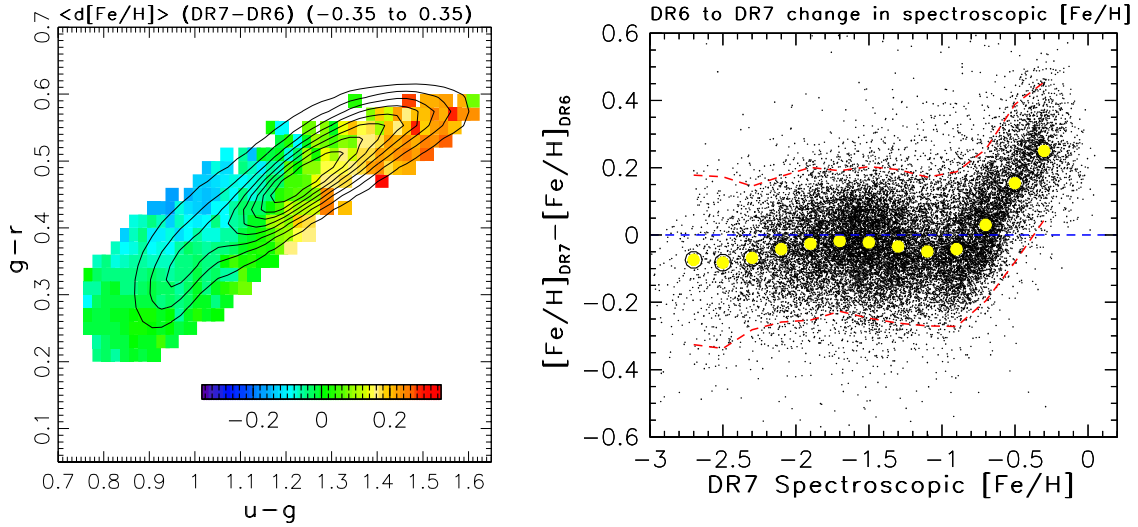
Fig. A1.— Summary of the differences between SDSS spectroscopic metallicity values distributed with Data Releases 6 and 7. The left panel shows the median difference between the DR7 and DR6 values for 0.02×0.02 mag^2 large bins in the $g - r$ vs. $u - g$ color-color diagram, color-coded according to the legend shown in the panel. The largest differences of $0.2 - 0.3$ dex are seen in the top right corner, which corresponds to high metallicities. The right panel shows the difference in metallicities as a function of the new DR7 values. Individual stars are shown as small dots, and the median values of the difference are shown as large circles. The two dashed lines mark the $\pm 2\sigma$ envelope around the medians, where σ is the root-mean-square scatter (~ 0.1 dex, due to software updates) estimated from the interquartile range. The median differences are larger than 0.1 dex only at the high-metallicity end ($[Fe/H] > -0.6$).
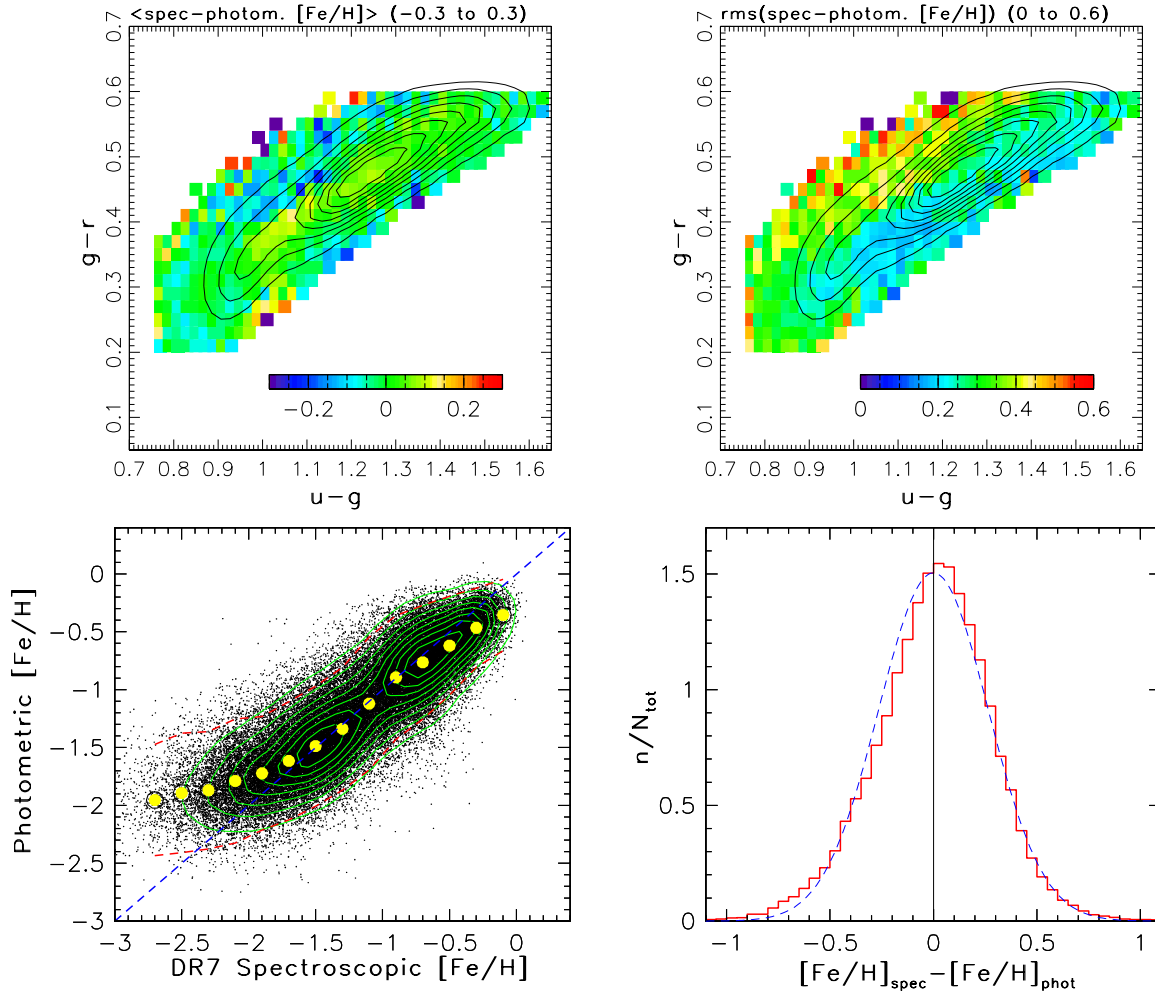
Fig. A2.— Color-coded map in the top left panel shows the median difference between spectroscopic and revised photometric metallicities for $\sim 50,000$ stars from SDSS Data Release 7. The median value is zero and the root-mean-square scatter is 0.07 dex. The contours show the distribution of stars with $r < 20$ and at high Galactic latitudes. The top right panel shows the root-mean-square scatter of the difference between spectroscopic and photometric metallicities in each pixel. The top two panels are analogous to the bottom two panels in figure 2 from I08. The bottom left panel shows the photometric metallicity as a function of the spectroscopic metallicity. Individual stars are shown by small dots, and the median values of the difference are shown by large circles. The distribution of stars is shown as linearly spaced contours. Note that the photometric metallicity saturates at $[Fe/H] \sim -2$ at the low-metallicity end. The histogram in the bottom right panel shows the distribution of the difference between spectroscopic and photometric metallicities for stars with spectroscopic metallicity, $[Fe/H] > -2.2$. A best-fit Gaussian centered on zero and with a width of 0.26 dex is shown by the dashed line.
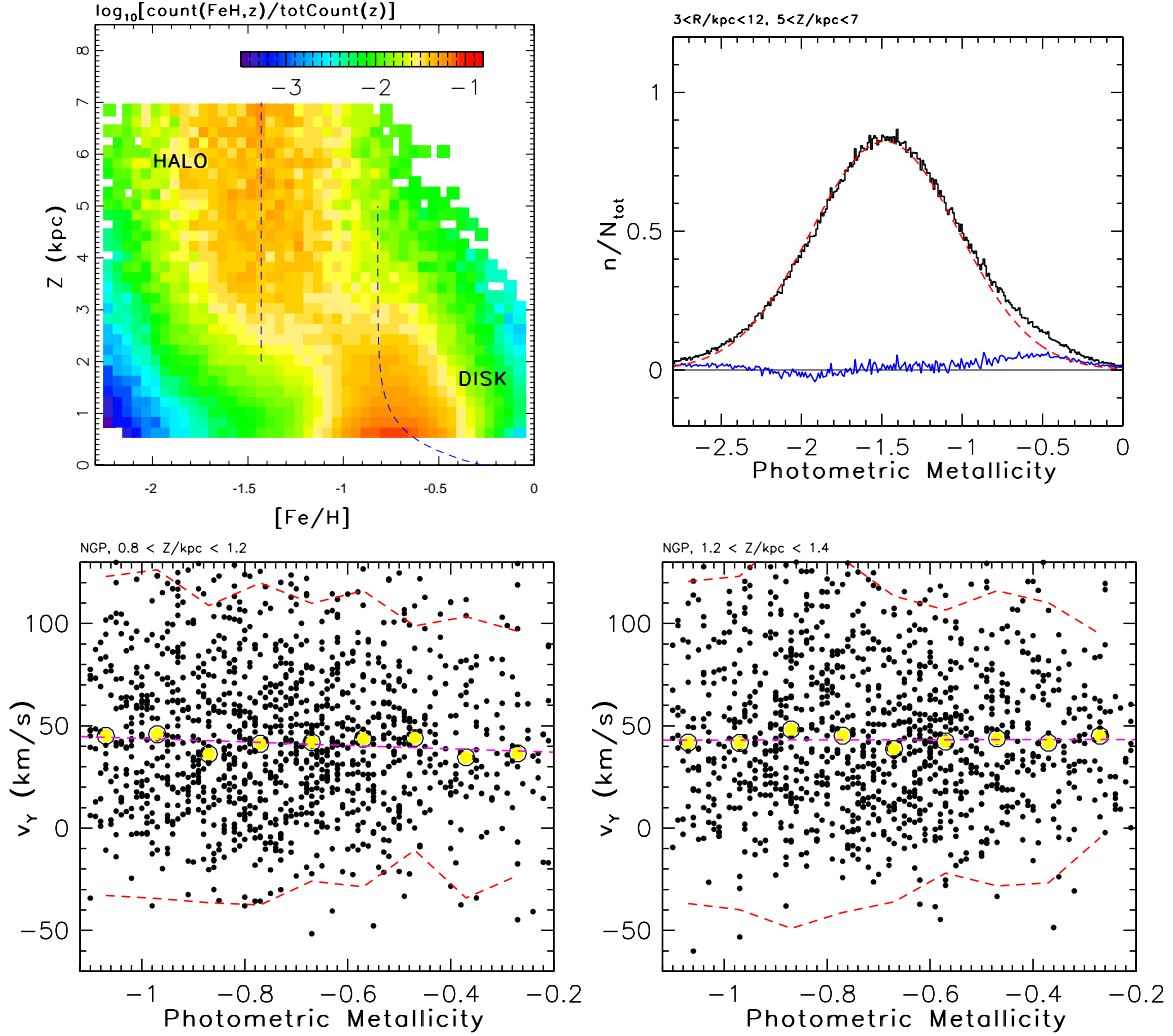
Fig. A3.— The top left panel shows the conditional metallicity distribution as a function of distance from the Galactic plane, and is analogous to the bottom left panel of figure 9 from I08. Note that the new photometric metallicities include $[Fe/H] > -0.4$. The dashed line, which shows the median disk metallicity, is also revised (see text). The top right panel is analogous to figure 10 from I08 and shows the metallicity distribution for stars with $5 < Z < 7$ kpc, where Z is the distance from the Galactic plane. Note that the photometric metallicity artifact at $[Fe/H] = -0.5$ discussed by I08 is no longer present. However, there is still evidence that disk stars exist at such large distances from the plane. The bottom two panels show the heliocentric rotational velocity for disk stars in two thin Z slices, and are analogous to the bottom right panel in figure 16 from I08. Note that the correlation between velocity and metallicity is still absent.
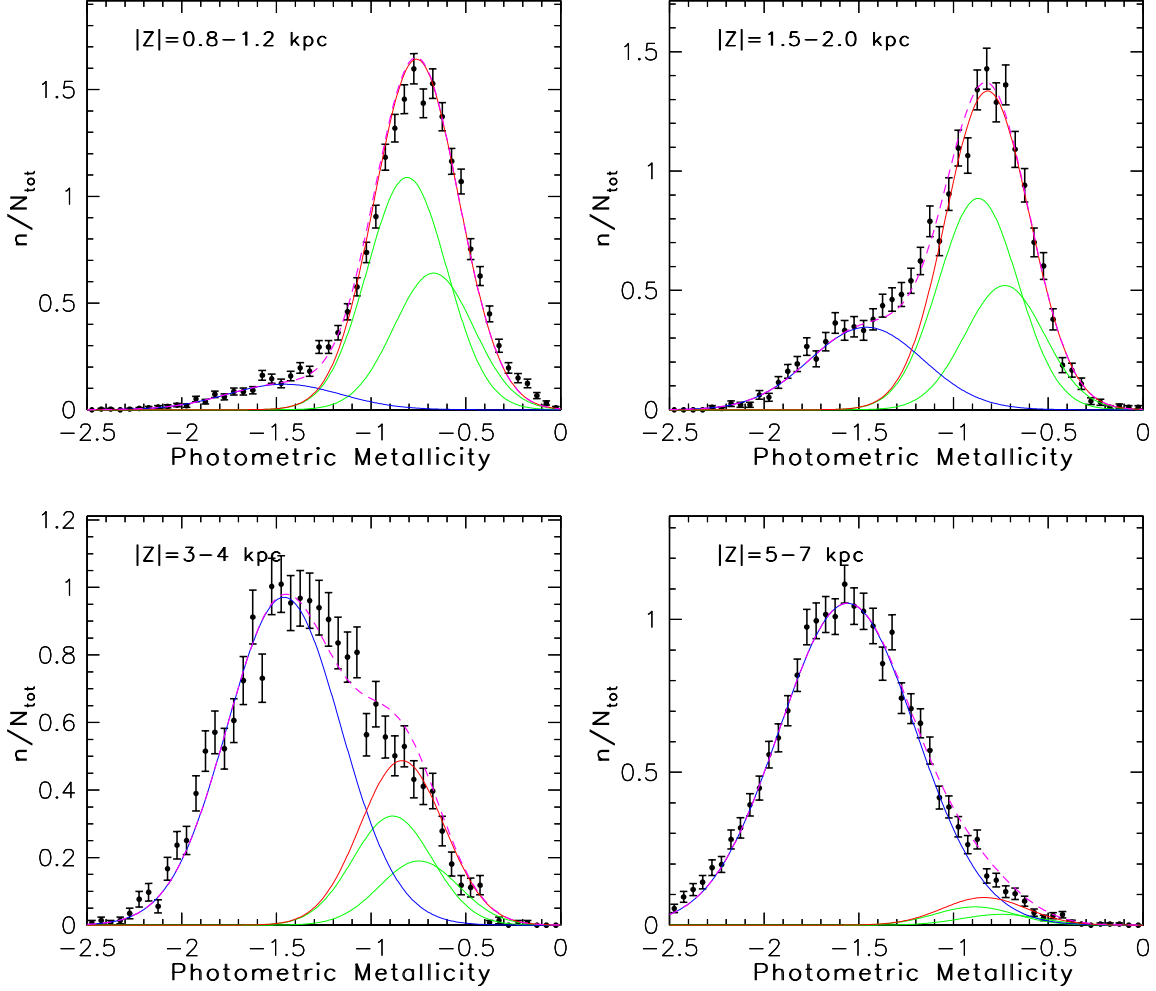
Fig. A4.— Analogous to figure 7 from I08. The symbols with error bars show the metallicity distribution for stars with $0.2 < g - r < 0.4$, $7 < R < 9$ kpc and distances from the galactic plane as marked, where R is the galactic cylindrical radius. The behavior is qualitatively similar to that seen in I08. The only significant quantitative difference is in the model for the metallicity distribution of disk stars (see text).